Large-Eddy-Simulation of Reynolds Stress Budgets in and above Forests in Neutral Atmospheric Boundary Layers

Hong-Bing Su[1] • Kyaw Tha Paw U[2]

Received: 6 January 2022/ Accepted: DD Month YEAR/ Published online: DD Month YEAR

Abstract

Large-eddy simulations (LESs) of inversion-capped neutral atmospheric boundary layers (ABLs) are augmented to earlier small-domain LESs of a sparse forest and field observation to evaluate the budgets of all non-negligible resolved-scale Reynolds stress components. The focus is on the atmospheric surface layer comprised of the roughness sublayer (RSL) in and above horizontally homogeneous forests and the inertial sublayer (ISL) above the RSL over flat terrain. The greater LES domain and ABL depths result in greater depths of both the RSL and the ISL. A key result is that in the upper portions of the canopy and above, pressure redistribution is a major sink of normal stress in the horizontal direction with mean shear production as a major source, whereas in the horizontal direction absent of mean shear production and in the vertical direction, pressure redistributions are major sources of normal stresses. In the lower portions of the canopy where mean shear production and turbulent transport are much reduced, pressure redistributions are major sources of horizontal velocity variances but a major sink of vertical velocity variance. Pressure transport is a greater source of vertical velocity variance than turbulent transport from the ground level to just under the treetops where it transitions to a major sink up to about 1.5 times canopy height. This greater significance of pressure transport over turbulent transport increases with increased vegetation area index (*VAI*). The impact of increased geostrophic wind speed is negligible compared to that of increased *VAI* on enhancing normalized budget terms in the vicinity of treetops.

✉ Hong-Bing Su
suh@ecu.edu

[1] Department of Geography, Planning, and Environment, East Carolina University, Greenville, NC 27858-4353, USA

[2] Department of Land, Air and Water Resources, University of California, Davis, CA 95616, USA

Keywords Forest • Large-eddy-simulation • Pressure-gradient interaction • Reynolds stress budgets • Roughness sublayer

1 Introduction

It has been three decades since the pioneering work by Shaw and Schumann (1992) using large-eddy simulation (LES) to study airflow in and above horizontally homogeneous forest canopies on flat ground. Since that time LES has been applied to many roughness surface types, including various plant canopies, topographies, and cities. Some of these studies have been for heterogeneous surfaces, such as windbreaks, forest edges, forest clearings, patches, leaf area index (*LAI*) inhomogeneity, and vineyards (Patton et al. 1998; Albertson et al. 2001; Yang et al. 2006a, 2006b, 2006c; Dupont and Brunet 2008a, 2009; Cassiani et al. 2008; Bohrer et al. 2009; Dupont et al. 2011, 2012; Huang et al. 2011; Schlegel et al. 2012, 2015; Chahine et al. 2014; Lopes et al. 2015; Boudreault et al. 2017; Nakao and Hattori 2019; Ma et al. 2020). A comprehensive survey of LES studies of airflow in and above horizontally heterogeneous plant canopies and flows associated with plant canopies on hilly terrain and urban structures (Dupont et al. 2008; Patton and Katul 2009; Ross 2011; Giometto et al. 2016; Liu et al. 2019; Nazarian et al. 2020; Blunn et al. 2022) is beyond the scope of this paper.

For horizontally homogeneous plant canopies on flat ground, which is the situation for this study, previous LES studies have investigated various aspects of airflow in and above plant canopies. These include the effects of vegetation area density (Shaw and Schumann 1992; Dupont and Brunet 2008b; Huang et al. 2009) and thermal stability (Shaw and Schumann 1992; Nebenführ and Davidson 2015; Patton et al. 2016), validating single-point (Su et al. 1998a) and two-point (Su et al. 2000) turbulent statistics against field observations, diffusion and dispersion from continuous sources in plant canopies (Su and Leclerc 1998; Pan et al. 2014a), the flexibility of plants (Dupont et al. 2010; Pan et al. 2014b), the failure of *K* theory (Banerjee et al. 2017), and the characterization of coherent structures (Kanda and Hino 1994; Su et al. 2000; Fitzmaurice et al. 2004; Watanabe 2004, 2009; Finnigan et al. 2009; Huang et al. 2009; Gavrilov et al. 2013; Bailey and Stoll 2016). Shaw and Patton (2003) concluded that it is unnecessary to carry a prognostic equation for the wake energy in the LES of airflow in forest canopies despite wake energy being comparable in magnitude with subgrid-scale (SGS) kinetic energy resulting from the cascade of the resolved-scale kinetic energy. Patton et al. (2003) studied the influence of a forest on top-down and bottom-up diffusion in a convective boundary layer using two-way nesting LES (Sullivan et al. 1996).

The primary motivation of the present work is to use the LESs to evaluate the budgets of all important Reynolds stress components in the atmospheric surface layer that is comprised of the roughness sublayer (RSL) in and above forests and the inertial sublayer (ISL) above the RSL, in inversion-capped neutral atmospheric boundary layers (ABLs). Similar analyses have been carried out for a neutral ABL (Andrén and Moeng 1993), and cloud-topped ABLs (Heinze et al. 2015), in which the surface layer is poorly resolved and the RSL is not explicitly resolved. To our knowledge, LES evaluation of the budgets of all Reynolds stress components in the RSL in and above plant canopies are still largely missing in the literature. Only the budgets of turbulent kinetic energy (TKE) (Dwyer et al. 1997; Shen and Leclerc 1997; Yue et al. 2008; Nebenführ and Davidson 2015; Watanabe et al. 2020) or tangential shear stress (Shen and Leclerc 1997; Dupont et al. 2011) have been evaluated. This is also the case in laboratory experiments (Raupach et al. 1986; Brunet et al. 1994; Nepf and Vivoni 2000; Poggi et al. 2004; Yue et al. 2008) and in situ observations (Shaw and Seginer 1985; Leclerc et al. 1990; Meyers and Baldocchi 1991; van Hout et al. 2007). Dupont et al. (2012) presented the budgets of vertical and streamwise velocity variances deep into a pine stand from the edge region, but the budget of spanwise or crosswind velocity variance was absent. A contribution the LES can make is to quantify the pressure-gradient interactions (Wyngaard 2010) in Reynolds stress budgets that have been extremely difficult, if not impossible to measure in the laboratory and field (Maitani and Seo 1985; Shaw et al. 1990). We will evaluate the parametrizations of the pressure-gradient interaction (including pressure redistribution and pressure transport) in a companion paper. This split is similar to Heinze et al. (2015) and (2016) for cloud-topped ABLs. Perret and Patton (2021) used a multiscale decomposition to quantify the interscale transfer of TKE and Reynolds shear stress between the larger resolved scales in the ABL and the smaller resolved scales near the canopy top. This is different from the typical decomposition (horizontal mean and departure from it) used in this study, which does not separate contributions between large and small resolved eddies.

Our first analyses on these topics were reported in a doctoral dissertation (Su 1997) and a conference paper (Su et al. 1998b). A question that has remained since is how the results may be impacted by the limited domain in that early LES, which is 9.6 and 3 times of canopy height (h_c) in the horizontal and vertical directions, respectively. This was typical in the earlier LESs of airflow in and above plant canopies (Shaw and Schumann 1992; Kanda and Hino 1994; Dwyer et al. 1997; Shen and Leclerc 1997; Su et al. 1998a; Shaw and Patton 2003; Fitzmaurice et al. 2004). Su et al. (2000) used a domain size twice as large or grid spacing half of those in Su et al. (1998a) in both the vertical and horizontal directions. However, those simulations have not been used to evaluate Reynolds stress and their budgets, which is addressed as part of the work presented here. Increasingly larger LES domains (normalized by h_c) have been used in later studies (Watanabe 2004, 2009; Yue et al. 2007; Dupont and Brunet 2008b; Finnigan et al. 2009; Huang et al. 2009; Dupont et al. 2010; Gavrilov et al. 2013; Nebenführ and Davidson 2015; Bailey and Stoll 2016), but only a few used a large enough vertical domain to allow realistic ABL depths (Patton et al. 2003; Patton et al. 2016; Banerjee et al. 2017). In this study, four LES cases with a large domain (50 h_c in the horizontal and 77 h_c in the vertical) while maintaining the same fine grid resolution as our earlier small-domain LESs are augmented to study the impacts of different vegetation area index (*VAI*) and external pressure-gradient force. These simulations yielded much greater ABL depths, which allowed us to study whether a logarithmic layer or the ISL survives above the RSL (Jiménez 2004), and the depths of both the RSL and the ISL.

A description of the four large-domain LES cases and their differences with the four earlier small-domain LES runs are given in Sect. 2, along with the budget equations for the resolved-scale Reynolds stress. In Sect. 3, we first present and contrast profiles of mean winds and Reynolds stress components in two different horizontal coordinates, including the depths of both the RSL and the logarithmic layer or ISL. We then discuss the Reynolds stress budgets in two different horizontal coordinates, and the effects of vegetation density and its vertical distribution, geostrophic wind speed, LES domain size, and grid spacing.

2 Methodology

2.1 Large-Eddy Simulations

The LES explicitly resolves the temporal evolutions of spatially filtered velocity $\langle u_i \rangle$, the virtual potential temperature $\langle \theta \rangle$, the kinematic static pressure $\langle p \rangle$ (a deviation from the horizontal mean kinematic static pressure P/ρ_0) in which ρ_0 is a reference air density, and subfilter-scale (SFS) kinetic energy $\langle e \rangle$, over a three-dimensional array of grids by solving the following set of equations:

$$\frac{\partial \langle u_i \rangle}{\partial t} = -\frac{\partial \langle u_i \rangle \langle u_j \rangle}{\partial x_j} - \frac{1}{\rho_0}\frac{\partial P}{\partial x_i} + \frac{g}{\theta_0}\langle \theta \rangle \delta_{i3} - \frac{\partial \langle p^* \rangle}{\partial x_i} - \frac{\partial \tau_{ij}}{\partial x_j} - 2\Omega_j \epsilon_{ijk} \langle u_k \rangle + F_i, \tag{1}$$

$$\frac{\partial \langle \theta \rangle}{\partial t} = -\frac{\partial \langle \theta \rangle \langle u_j \rangle}{\partial x_j} - \frac{\partial \tau_{\theta j}}{\partial x_j}, \tag{2}$$

$$\frac{\partial \langle u_j \rangle}{\partial x_j} = 0, \tag{3}$$

$$\frac{\partial^2 \langle p^* \rangle}{\partial x_i^2} = \frac{\partial}{\partial x_i}\left\{ -\frac{\partial \langle u_i \rangle \langle u_j \rangle}{\partial x_j} + \frac{g}{\theta_0}\langle \theta \rangle \delta_{i3} - \frac{\partial \tau_{ij}}{\partial x_j} - 2\Omega_j \epsilon_{ijk} \langle u_k \rangle + F_i \right\}, \tag{4}$$

$$\frac{\partial \langle e \rangle}{\partial t} = -\frac{\partial \langle e \rangle \langle u_j \rangle}{\partial x_j} - \tau_{ij}\frac{\partial \langle u_i \rangle}{\partial x_j} - \frac{g}{\theta_0}\tau_{\theta j}\delta_{i3} + \frac{\partial}{\partial x_i}\left(2k_m \frac{\partial \langle e \rangle}{\partial x_i} \right) - \varepsilon - \varepsilon_{fd}, \tag{5}$$

where t is time; g is gravitational acceleration; $x_i = (x_1, x_2, x_3) = (X, Y, Z)$ are the local Cartesian coordinates with the positive (X, Y, Z) pointing to the east, north and upwards, respectively (Holton and Hakim 2012); $u_i = (u_1, u_2, u_3) = (U, V, W)$ are corresponding velocities; $\Omega_j = \Omega(0, \cos\phi, \sin\phi)$ are the angular velocity components of the Earth with Ω being the angular speed of the Earth and ϕ being the latitude; θ_0 is a reference virtual potential temperature; δ_{ij} denotes the Kronecker delta; and ϵ_{ijk} denotes the Levi-Civita tensor. The Einstein summation convention for repeated indices is applied. An angular bracket denotes a resolved-scale (or filtered) variable with a double prime indicating an SFS fluctuation. Like in previous LESs of horizontally homogeneous ABLs over flat terrains (Moeng 1984), the resolved-scale vertical velocity $\langle W \rangle$ is a deviation from the hydrostatic balance and the horizontal average (denoted by an overbar). At each time step in the LES code, $\overline{\langle W \rangle} = 0$ is enforced by removing the horizontal average of the vertical component of the right-hand side (r.h.s) of (1) at all altitudes. This is also applied to (4).

The anisotropic (deviatoric) part of the SFS stress tensor is defined and parametrized as in Moeng (1984), $\tau_{ij} = S_{ij} - \delta_{ij} S_{kk}/3 = -k_m\left(\partial\langle u_i\rangle/\partial x_j + \partial\langle u_j\rangle/\partial x_i\right)$, in which the total SFS stress tensor is defined as $S_{ij} = \langle u_i'' u_j''\rangle + \langle u_i''\langle u_j\rangle\rangle + \langle\langle u_i\rangle u_j''\rangle$, and k_m is the SFS eddy diffusivity for momentum. The isotropic part of the SFS stress $S_{kk}/3 = 2\langle e\rangle/3$ is combined with $\langle p\rangle$ in defining $\langle p^*\rangle = \langle p\rangle + 2\langle e\rangle/3$ (Deardorff 1972; Moeng 1984; Pope 2000; Wyngaard 2010; Hanjalić and Launder 2011).

The SFS heat flux is parametrized as $\tau_{\theta j} = k_h\left(\partial\langle\theta\rangle/\partial x_j\right)$ with k_h being the SFS eddy diffusivity for heat. The parametrizations of k_m, k_h, and free-air dissipation ε can be found in Moeng (1984), Moeng and Wyngaard (1988): $k_m = C_k l\langle e\rangle^{1/2}$, $k_h = (1+2l/\Delta)k_m$, $\varepsilon = c_\varepsilon\langle e\rangle^{3/2}/l$, $\Delta = [(1.5\Delta X)(1.5\Delta Y)\Delta Z]^{1/3}$, $C_k = 0.1$, $c_\varepsilon = 0.93$, $l = \Delta$ except for stable stratification $l = 0.76\langle e\rangle^{1/2}[(g/\theta_0)(\partial\langle\theta\rangle/\partial Z)]^{-1/2}$, and ΔX, ΔY, ΔZ are grid mesh spacing.

The canopy form drag is parametrized as $F_i = -C_d a_p(\langle u_i\rangle\langle u_i\rangle)^{1/2}\langle u_i\rangle$ (Shaw and Schuman 1992), in which $C_d = 0.15$ is the drag coefficient derived from measurement inside the Camp Borden forest (Su et al. 1998a), and a_p represents one-sided leaf area density in the deciduous forest at Camp Borden (Neumann et al. 1989) and in LES Runs A–D (Su et al. 1998a, 2000) or projected (frontal) vegetation area density in LES Cases 1–4. The effects of wind speed (Su et al. 2008) and streamlining (Rudnicki et al. 2004; Vollsinger et al. 2005; Pan et al. 2014b) on C_d are not considered, nor are the effects of volume and aperture restriction in semi-porous barriers like a forest (Chatziefstratiou et al. 2014). This is a much simpler treatment than resolving fine-scale plant structure in a corn canopy (Yue et al. 2007), or parametrizing the drag force of fractal trees using the renormalized numerical simulation technique (Graham and Meneveau 2012), or numerically treating fractal trees as immersed boundaries (Schröttle and Dörnbrack 2013). Following Shaw and Patton (2003), the conversion of $\langle e\rangle$ to wake-scale kinetic energy is calculated as the work performed by SFS motions against the form drag $\varepsilon_{fd} = \frac{8}{3}C_d a_p(\langle u_i\rangle\langle u_i\rangle)^{1/2}\langle e\rangle$.

Four LES cases were performed using a domain of (1000 m, 1000 m, 1536 m) in the (X, Y, Z) directions with (500, 500, 768) uniform grids of (2 m)^3. The domain size, especially in the vertical, is significantly greater than those in Su et al. (2000). This allows us to examine the effects of limited vertical domain and the artificial momentum source at the top of the domain in our earlier LES (Su et al. 1998a). The numbers of three-dimensional grids (500, 500, 768) in this study are greater than (320, 320, 320) in Banerjee et al. (2017) but smaller than (2048, 2048, 1024) in Patton et al. (2016) which is beyond the computational resources available to us. The horizontal domains are greater, 71.4 h_c in Banerjee et al. (2017) and 250 h_c in Patton et al. (2016), but these two studies yielded smaller ABL depths than the present study as discussed later.

The near-neutral case in Patton et al. (2016) had a heat flux 0.24 K m s^{-1} (300 W m^{-2}) at the canopy top, which is not insignificant when compared to sensible heat flux observed over forests at many long-term carbon cycle study sites (e.g., Schmid et al. 2003). Pedersen et al. (2014) specifically discussed the impacts of surface heat fluxes on the differences between neutral and near-neutral ABLs. In comparison, the total heat fluxes by the forest canopies are 0.05 K m s^{-1} in Patton et al. (2003) and 0.18 K m s^{-1} in Banerjee et al. (2017) for their respective LESs of convective boundary layers. In our simulations, sensible heat fluxes at the ground surface and at the surfaces of forest elements are all zero. However, our simulated ABLs are not classic Ekman ABLs (Andrén and Moeng 1993) but are inversion-capped neutral ABLs with zero heat flux at the surface (Moeng and Sullivan 1994; Lin et al. 1997; Pedersen et al. 2014; Salesky et al. 2017; Berg et al. 2020).

Similar to Moeng and Sullivan (1994), the initial velocity field was set to the geostrophic wind (zero vertical velocity) throughout the LES domain. The initial values of $\langle\theta\rangle$ were set to 300 K below the height $Z = 500$ m $= 25\ h_c$ and increased above this height at a rate of 6 K km^{-1}. However, there are differences in the initial fields of $\langle\theta\rangle$ among the various LESs of inversion-capped neutral ABLs. Pedersen et al. (2014) and Berg et al. (2020) set up initial values of $\langle\theta\rangle$ increasing linearly from the bottom to the top of their LES domains at a rate of 3 K km^{-1} in Berg et al. (2020) and four different rates of (1, 3, 6, 10) K km^{-1} in Pedersen et al. (2014). These initially stable ABLs undoubtedly hindered and slowed down the growth of turbulence and the ABL depths, and contributed to longer simulation times to reach a quasi-equilibrium state. On the other hand, the final ABL heights after reaching a quasi-steady state in Moeng and Sullivan (1994), Salesky et al. (2017), and Banerjee et al. (2017) are near the altitudes where very large rates of increase in $\langle\theta\rangle$ with height (80–128 K km^{-1}) are initially set.

The external horizontal mean pressure-gradient forces are defined by the geostrophic wind $-(1/\rho_0)\,\partial P/\partial Y = f_c U_G$ and $-(1/\rho_0)\,\partial P/\partial X = -f_c V_G$. In this study, we set V_G to zero. The Coriolis parameter f_c is for the latitude of Howland, Maine, USA, where the four new LES cases were performed for a related field project. The model forests have a height (h_c) of 20 m with *VAI* ($m^2\ m^{-2}$) values of 2 and 6.5. The profiles of vegetation area density a_p ($m^2\ m^{-3}$) (Fig. 1) are similar to case2 in Dupont et al. (2008b) in their LES study of the influence of foliar density profile on canopy flow, as well as a fully leafed deciduous forest (Baldocchi and Meyers 1988).

Fully developed turbulent ABLs are achieved and the flow reached a quasi-steady state after 4.5 h of simulation time. This is slightly longer than the total simulation time in Moeng and Sullivan (1994) and the 4 h for reaching a quasi-steady state in Salesky et al. (2017), but shorter than those in Pedersen et al. (2014) and Berg et al. (2020) due to much stronger geostrophic winds and much rougher surface over tall forests in the present study. After reaching a quasi-steady state, each LES case was performed for an additional 1.5 h, and simulations over the last three large-eddy turnover times were saved every 1 min or 0.5 min for $U_G = 20$ or 40 m s^{-1}, respectively, for the analyses presented here. The mean wind profiles throughout the ABLs (Fig. 2a, b) are used to discuss the impact of horizontal coordinate rotation on Reynolds stress and their budgets. Additional full boundary-layer profiles of first- and second-order statistics, snapshots of *X*-*Z* and *X*-*Y* slides of turbulent streamwise and vertical velocities, and energy spectra, are provided in Appendix 1.

In addition to smaller domains, a number of differences in our earlier LESs (Su et al. 1998a, 2000) from the above four large-domain LES cases are noted here. First, there is no external horizontal pressure-gradient force and the airflow is driven by a momentum source at the top of the domain in the *X*-direction with a total strength equal to the sum of form drag imposed by the canopy at each time step. The artifacts due to this momentum source and the limited vertical domain in our earlier LESs on Reynolds stress and their budgets are the main concerns we have and aim to exam in this study. Second, the Coriolis force is neglected. All of these could impact the horizontal mean wind and subsequently the Reynolds stress. An example is that the constant momentum flux above the canopy in the earlier small-domain LES runs is absent in the 4 large-domain LES cases. Another example is the mean wind shear production of Reynolds stress discussed later. Third, the buoyancy force is zero and there is no capping inversion, therefore, the airflow is purely neutral. Fourth, the SFS kinetic energy includes both cascade of resolved-scale kinetic energy and wake production inside the canopy. The length-scale in SFS eddy diffusivity is reduced to 1/4 of that determined by grid spacing based on wake production being about 4 times of shear production of SFS kinetic energy. Fifth, only a sparse forest ($LAI = 2$) was studied with a different profile of a_p (Fig. 1). However, the four earlier LES runs did include a case with a smaller grid spacing. Finally, the model forest in the earlier LES runs also has a height (h_c) of 20 m.

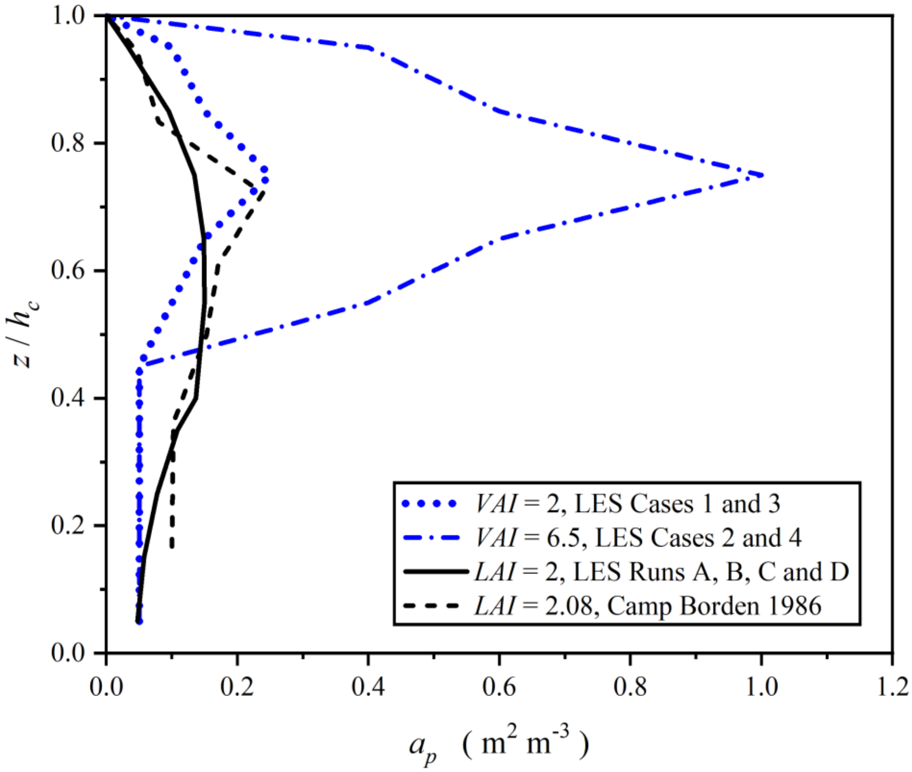

Fig. 1 Profiles of a_p representing one-sided leaf area density in the deciduous forest at Camp Borden (Neumann et al. 1989) and in LES Runs A−D (Su et al. 1998a, 2000) or projected (frontal) vegetation area density in LES Cases 1−4. The vertical integration of a_p through the canopy yields *LAI* or *VAI* (m^2 m^{-2})

The same field observations used in Su et al. (1998a, 2000) for comparing single- and two-point statistics in and above a deciduous forest near Camp Borden military base in Ontario, Canada, are used here to compare shear production, turbulent transport, and canopy form drag destruction in the budgets of Reynolds stress. Detailed descriptions of the site and experiment can be found in Shaw et al. (1988). The forest is primarily mixed hardwood with principle species being aspen and red maple. The average height of the forest was about 18 m. Turbulence data of velocities and temperature collected at 10 Hz from ultrasonic anemometer-thermometers (Kaijo Denki Co., Ltd.) at seven heights on two scaffolding-type towers were selected from day 280 (October 7) and day 281 (October 8) in 1986 when the wind came from directions with sufficient upwind fetch (~ 4 km). The leaf area density profile for day 281 ($LAI = 2.08$) is given in Fig.1. Five 30-min records of 10-Hz data under near-neutral conditions ($-0.05 < h_c/L < 0.01$) were used, where L is the Obukhov length calculated from measurements at the canopy top. Similar to Shaw et al. (1988), the averaging time is 30 min. A horizontal coordinate rotation was applied to force each 30-min mean lateral velocity to zero. A second coordinate rotation in the *x*-*z* plane to force the mean vertical velocity to zero was applied only to measurements above the canopy, because the presence of individual trees and branches can distort the flow and cause local non-zero mean vertical velocities (Baldocchi and Hutchinson 1987). Su et al. (1998a) applied linear detrending in their analyses and found it made negligible difference on calculated statistics.

2.2 Reynolds Stress Budgets

In the following, an overbar denotes a horizontal average and a prime indicating a deviation therefrom. However, all budget terms and turbulent statistics presented below are further averaged over samples saved every 1 min or 0.5 min for $U_G = 20$ or 40 m s^{-1} over the last three large-eddy turnover times of simulations to form quasi-steady-state statistics (Pedersen et al. 2014; Patton et al. 2016; Salesky et al. 2017; Berg et al. 2020). The Reynolds stress and kinetic energy are all kinematic, but the term "kinematic" is omitted in the rest of the paper for the sake of brevity.

The budget equation for the resolved-scale Reynolds stress tensor $\overline{\langle u_i \rangle' \langle u_k \rangle'}$ may be written as,

$$\frac{\partial \overline{\langle u_i\rangle'\langle u_k\rangle'}}{\partial t} = \underbrace{-\frac{\partial \overline{\langle u_i\rangle'\langle u_k\rangle'}\;\overline{\langle u_j\rangle}}{\partial x_j}}_{A_{ik}} \underbrace{-\frac{\partial \overline{\langle u_i\rangle'\langle u_k\rangle'\langle u_j\rangle'}}{\partial x_j}}_{T^r_{ik}} \underbrace{-\left(\overline{\langle u_i\rangle'\langle u_j\rangle'}\;\frac{\partial \overline{\langle u_k\rangle}}{\partial x_j} + \overline{\langle u_k\rangle'\langle u_j\rangle'}\;\frac{\partial \overline{\langle u_i\rangle}}{\partial x_j}\right)}_{P_{ik}}$$

$$\underbrace{+\left(\frac{g}{\theta_0}\overline{\langle u_i\rangle'\langle \theta\rangle'}\;\delta_{k3} + \frac{g}{\theta_0}\overline{\langle u_k\rangle'\langle \theta\rangle'}\;\delta_{i3}\right)}_{B_{ik}} \underbrace{-\,2\Omega_j\left(\epsilon_{kjm}\overline{\langle u_i\rangle'\langle u_m\rangle'} + \epsilon_{ijm}\overline{\langle u_k\rangle'\langle u_m\rangle'}\right)}_{C_{ik}}$$

$$\underbrace{-\left(\overline{\langle u_i\rangle' F_k'} + \overline{\langle u_k\rangle' F_i'}\right)}_{D_{ik}} \underbrace{-\left(\overline{\langle u_i\rangle'\frac{\partial \tau_{kj}'}{\partial x_j}} + \overline{\langle u_k\rangle'\frac{\partial \tau_{ij}'}{\partial x_j}}\right)}_{\Lambda_{ik}} \underbrace{-\left(\overline{\langle u_i\rangle'\frac{\partial \langle p^*\rangle'}{\partial x_k}} + \overline{\langle u_k\rangle'\frac{\partial \langle p^*\rangle'}{\partial x_i}}\right)}_{\Pi_{ik}}, \qquad (6)$$

where terms on the r.h.s represent advection by the mean wind A_{ik}, transport by the resolved-scale turbulence T^r_{ik}, mean-gradient production (Wyngaard 2010) or action by mean strain (Hanjalić and Launder 2011) P_{ik}, buoyancy effect B_{ik}, Coriolis effect C_{ik}, destruction by form drag due to forest elements D_{ik} (Su et al. 1997), the anisotropic part of SFS-stress-gradient interaction Λ_{ik} , and a modified pressure-gradient interaction (Wyngaard 2010) or velocity-pressure-gradient tensor Π_{ik} (Pope 2000). The term modified is used here because $\langle p^*\rangle = \langle p\rangle + 2\langle e\rangle/3$ so that Π_{ik} is the sum of the pressure-gradient interaction $\Pi_{ik}^{<p>}$ due to $\langle p\rangle$ and the isotropic-SFS-stress-gradient interaction $\Pi_{ik}^{<e>}$ due to $S_{kk}/3 = 2\langle e\rangle/3$. The sum of the r.h.s of (6) is denoted by Σ_{ik}. For horizontally homogeneous forests in inversion-capped neutral ABLs, A_{ik} is zero, B_{ik} and C_{ik} are negligible. These three terms will not be shown or further discussed in the results below.

The anisotropic part of the SFS-stress-gradient interaction Λ_{ik} may be decomposed into two parts,

$$\Lambda_{ik} = \underbrace{-\left(\frac{\partial \overline{\langle u_k\rangle'\tau_{ij}'}}{\partial x_j} + \frac{\partial \overline{\langle u_i\rangle'\tau_{kj}'}}{\partial x_j}\right)}_{T^s_{ik}} \underbrace{+\left(\overline{\tau_{ij}'\frac{\partial \langle u_k\rangle'}{\partial x_j}} + \overline{\tau_{kj}'\frac{\partial \langle u_i\rangle'}{\partial x_j}}\right)}_{I_{ik}}, \qquad (7)$$

where T^s_{ik} may be interpreted as transport by anisotropic SFS stress, and I_{ik} represents interscale transfer from the resolved scales to the subfilter scales (Wyngaard 2010). If a prognostic equation for τ_{ij} is solved in an LES (Deardorff 1973a, 1973b), $-I_{ik}$ would appear in this equation.

A similar decomposition may be written for the isotropic part of the SFS-stress-gradient interaction. However, in incompressible airflow, a term equivalent to the non-transport second term on the r.h.s of (7) is zero in the budget of the resolve-scale TKE, even though we have found that this term can be either positive or negative in the budgets of the resolved-scale normal stresses. That is, this term does not transfer kinetic energy from the resolved scales to the subfilter scales, and only redistributes the resolved-scale kinetic energy among normal stress components. This is the primary rationale to combine $\Pi_{ik}^{<e>}$ with $\Pi_{ik}^{<p>}$ as the modified pressure-gradient interaction Π_{ik} in (6). This is not done in the earlier small-domain LES study of TKE budget in and above forests (Dwyer et al. 1997). However, we also found that transport by the isotropic part of SFS-stress is much smaller than that by $\langle p \rangle$ in the budget of vertical velocity variance and TKE, which is in agreement with Dwyer et al. (1997). It is noted that the pressure transport is zero in the budget of horizontal velocity variance due to horizontal homogeneity.

The classic decomposition of the pressure-gradient interaction term Π_{ik} is,

$$\Pi_{ik} = \underbrace{-\left(\frac{\partial \overline{\langle u_i \rangle' \langle p^* \rangle'}}{\partial x_k} + \frac{\partial \overline{\langle u_k \rangle' \langle p^* \rangle'}}{\partial x_i}\right)}_{T_{ik}^p} + \underbrace{\left(\overline{\langle p^* \rangle' \frac{\partial \langle u_i \rangle'}{\partial x_k}} + \overline{\langle p^* \rangle' \frac{\partial \langle u_k \rangle'}{\partial x_i}}\right)}_{R_{ik}}, \tag{8}$$

where the divergence of pressure flux part T_{ik}^p may be interpreted as transport by pressure fluctuations, the trace-free or deviatoric part R_{ik} represents redistribution by pressure fluctuations and has been termed energy redistribution (Rotta 1951; Mellor 1973), tendency-towards-isotropy (Donaldson 1973), return-to-isotropy (Stull 1988), pressure strain (Launder et al. 1975), pressure-rate-of-strain tensor (Pope 2000), and in the budgets of velocity variances or normal stresses, the intercomponent TKE transfer (Wyngaard 2010). This decomposition was used in the more recent work by Heinze et al. (2016) in their LES study of cloud-topped ABLs in which R_{ik} is called the pressure-scrambling term. Both the second-order closure models for canopy flows developed by Wilson and Shaw (1977) and by Wilson (1988) used this decomposition as they followed the work by Mellor (1973) and by Launder et al. (1975), respectively.

Lumley (1975) argued that the above customary decomposition is not unique and likely a wrong choice. It was proposed that the most natural definition of the deviatoric part of Π_{ik} seemed to simply subtract the trace (Lumley and Khajeh-Nouri 1975; Lumley 1979),

$$\Pi_{ik} = \underbrace{\Pi_{ik} + \frac{2}{3}\frac{\partial \overline{\langle u_j \rangle' \langle p^* \rangle'}}{\partial x_j}\delta_{ik}}_{R_{ik}^L} \underbrace{- \frac{2}{3}\frac{\partial \overline{\langle u_j \rangle' \langle p^* \rangle'}}{\partial x_j}\delta_{ik}}_{T_{ik}^L}, \tag{9}$$

where R_{ik}^{L} and T_{ik}^{L} represent the deviatoric part and the transport term in this decomposition (denoted by the superscript L), respectively. This decomposition was used in the LES of a neutrally stratified ABL (Andrén and Moeng 1993), and in the third-order closure model for airflow in and above plant canopies (Meyers and Paw U 1986). It was also evaluated by Su (1997) and Su et al. (1998b) for the resolved-scale Reynolds stress using the small-domain LES of airflow in and above a sparse forest (Su et al. 1998a).

Another decomposition was proposed by Mansour et al. (1988) but here only written for the resolved-scale flow field,

$$\Pi_{ik} = \underbrace{\Pi_{ik} + \frac{\overline{\langle u_i\rangle'\langle u_k\rangle'}}{\overline{\langle E\rangle}}\frac{\partial\overline{\langle u_j\rangle'\langle p^*\rangle'}}{\partial x_j}}_{R_{ik}^{M}} \underbrace{- \frac{\overline{\langle u_i\rangle'\langle u_k\rangle'}}{\overline{\langle E\rangle}}\frac{\partial\overline{\langle u_j\rangle'\langle p^*\rangle'}}{\partial x_j}}_{T_{ik}^{M}}, \qquad (10)$$

where $\overline{\langle E\rangle} = \overline{\langle u_i\rangle'\langle u_i\rangle'}/2$ is the resolved-scale TKE, R_{ik}^{M} is the deviatoric part, and T_{ik}^{M} represents transport in this decomposition (denoted by the superscript M).

Groth (1991) argued that as the starting point of many turbulence models, the transport equations for the Reynolds stress must be written in an unambiguous way and all terms ought to be given correct physical interpretation. By considering Newton’s second law for an infinitesimal cube volume of fluid with uniform and constant density, Groth (1991) demonstrated that the classic decomposition (8) be the appropriate choice. Moreover, both decompositions (9) and (10) have an obvious flaw in assigning non-zero pressure transport in homogeneous directions, which are the horizontal directions in this study.

Here, we propose the following decomposition,

$$\Pi_{ik} = \underbrace{\Pi_{ik} + \left(\frac{\partial\overline{\langle u_i\rangle'\langle p^*\rangle'}}{\partial x_k} + \frac{\partial\overline{\langle u_k\rangle'\langle p^*\rangle'}}{\partial x_i}\right)\delta_{ik}}_{R_{ik}^{*}} \underbrace{- \left(\frac{\partial\overline{\langle u_i\rangle'\langle p^*\rangle'}}{\partial x_k} + \frac{\partial\overline{\langle u_k\rangle'\langle p^*\rangle'}}{\partial x_i}\right)\delta_{ik}}_{T_{ik}^{*}}, \qquad (11)$$

where R_{ik}^{*} is the deviatoric part and T_{ik}^{*} represents the pressure transport term, respectively. For tangential Reynolds shear stress, this decomposition (denoted by the superscript *) is the same as Lumley’s decomposition (9) such that the transport term is zero, which we found to work better than the classic decomposition (8) in the RSL. However, for the normal stresses, this decomposition is the same as the classic decomposition (8) such that pressure transport is zero in the homogeneous (horizontal) directions, hence it does not have the flaw criticized by Groth (1991) and suffered by Lumley's decomposition (9) and by Mansour's decomposition (10).

Table 1 Model parameters and flow statistics for the 4 large-domain LES cases. Calculated at the canopy top are the horizontal mean wind velocity $\overline{\langle u \rangle}_{h_c}$, the horizontal mean wind directional angle α_{h_c}, the turbulent shear length scale L_s, the friction velocity u_*, and the bulk drag coefficient C_D. Estimates of the zero-plane displacement height d and the roughness length z_0 are explained in Sect. 3.1. The ABL height z_i determined by the maximum $\partial\overline{\langle \theta \rangle}/\partial z$ is followed by its value based on the peak negative heat flux in a parenthesis. The total velocity variances are $\overline{u'^2} = \overline{\langle u \rangle'^2} + \bar{\tau}_{xx} + 2\overline{\langle e \rangle}/3$, $\overline{v'^2} = \overline{\langle v \rangle'^2} + \bar{\tau}_{yy} + 2\overline{\langle e \rangle}/3$, and $\overline{w'^2} = \overline{\langle w \rangle'^2} + \bar{\tau}_{zz} + 2\overline{\langle e \rangle}/3$

Variable (unit)	Case 1	Case 2	Case 3	Case 4
VAI (m^2 m^{-2})	2	6.5	2	6.5
U_G (m s^{-1})	20	20	40	40
$\overline{\langle u \rangle}_{h_c}$ (m s^{-1})	2.70	2.20	4.44	3.79
α_{h_c} (°)	46.3	44.4	38.2	37.8
L_s/h_c	0.33	0.15	0.33	0.15
u_* (m s^{-1})	0.95	0.91	1.57	1.59
C_D	0.12	0.17	0.13	0.18
d/h_c	0.82	0.93	0.81	0.93
z_0/h_c	0.15	0.13	0.15	0.14
z_i/h_c	51.3(35.9)	52.6(39.1)	64.5(41.6)	64.4(36.8)
Logarithmic layer	2.9–5.6h_c	2.3–3.3h_c	2.7–5.4h_c	2.8–4.2h_c
$\overline{u'^2}/u_*^2$ at $z/h_c = 1$	2.98	2.94	3.10	3.00
$\overline{\langle u \rangle'^2}/u_*^2$ at $z/h_c = 1$	2.81	2.71	2.93	2.77
$\overline{v'^2}/u_*^2$ at $z/h_c = 1$	1.46	1.27	1.51	1.35
$\overline{\langle v \rangle'^2}/u_*^2$ at $z/h_c = 1$	1.29	1.04	1.34	1.13
$\overline{w'^2}/u_*^2$ at $z/h_c = 1$	1.07	0.90	1.07	0.90
$\overline{\langle w \rangle'^2}/u_*^2$ at $z/h_c = 1$	0.88	0.61	0.87	0.61
$\overline{u'^2}/u_*^2$ at $z/h_c = 2$	3.63	3.77	4.07	4.25
$\overline{\langle u \rangle'^2}/\mathrm{u}_*^2$ at $z/h_c = 2$	3.44	3.56	3.88	4.05
$\overline{v'^2}/u_*^2$ at $z/h_c = 2$	2.37	2.44	2.40	2.69
$\overline{\langle v \rangle'^2}/u_*^2$ at $z/h_c = 2$	2.19	2.23	2.21	2.49
$\overline{w'^2}/u_*^2$ at $z/h_c = 2$	1.59	1.69	1.57	1.68
$\overline{\langle w \rangle'^2}/u_*^2$ at $z/h_c = 2$	1.41	1.48	1.39	1.48

Wilson and Shaw (1977) followed Mellor (1973) in omitting the pressure flux $\overline{\langle u_i \rangle' \langle p^* \rangle'}$ because of poor understanding of it or by assuming it is negligibly small (Hanjalić and Launder 1972). Wilson (1988) also neglected the pressure transport term T_{ik}^p following

Launder et al. (1975). On the other hand, Meyers and Paw U (1986) simply followed Zeman and Lumley (1976) to parameterize the pressure flux in the equations of normal stresses by excluding the rapid part of pressure perturbation, with the simplest invariant model $\overline{\langle u_i\rangle'\langle p^*\rangle'} = -0.2\overline{\langle u_k\rangle'\langle u_k\rangle'\langle u_i\rangle'}$. However, some assumptions (e.g., homogeneous turbulence) used to derive this parametrization, including the coefficient 0.2 (Lumley 1979), are likely invalid for airflow in the RSL within and above plant canopies.

Table 2 Model parameters and flow statistics for the 4 earlier small-domain LES runs (Su et al. 1998a, 2000). All 4 LES runs have the same model forest with a height h_c of 20 m and an *LAI* of 2 (Fig. 1)

Variable (unit)	Run A	Run B	Run C	Run D
Domain size (L_x, L_y, L_z) (m)	(192, 192, 60)	(192, 192, 120)	(192, 192, 60)	(384, 384, 120)
Number of grids (N_x, N_y, N_z)	(96, 96, 30)	(96, 96, 60)	(192, 192, 60)	(192, 192, 60)
$\overline{\langle u\rangle}_{h_c}$ (m s^{-1})	0.95	0.93	0.96	1.00
L_s/h_c	0.64	0.67	0.43	0.70
u_* (m s^{-1})	0.27	0.28	0.28	0.31
C_D	0.08	0.09	0.08	0.10
d/h_c	0.75	0.75	0.73	0.74
z_0/h_c	0.09	0.11	0.09	0.12
Logarithmic layer	1.4–1.6h_c	1.7–2.1h_c	1.4–1.7h_c	1.8–2.6h_c
$\overline{u'^2}/u_*^2$ at $z/h_c = 1$	3.26	3.49	3.38	3.78
$\overline{\langle u\rangle'^2}/u_*^2$ at $z/h_c = 1$	2.95	3.01	3.07	3.32
$\overline{v'^2}/u_*^2$ at $z/h_c = 1$	1.65	1.85	1.71	1.88
$\overline{\langle v\rangle'^2}/u_*^2$ at $z/h_c = 1$	1.33	1.37	1.39	1.42
$\overline{w'^2}/u_*^2$ at $z/h_c = 1$	1.35	1.52	1.46	1.48
$\overline{\langle w\rangle'^2}/u_*^2$ at $z/h_c = 1$	1.03	1.05	1.12	1.03
$\overline{u'^2}/u_*^2$ at $z/h_c = 2$	3.94	3.67	4.03	4.40
$\overline{\langle u\rangle'^2}/\mathrm{u}_*^2$ at $z/h_c = 2$	3.56	3.40	3.79	4.16
$\overline{v'^2}/u_*^2$ at $z/h_c = 2$	2.16	2.10	2.07	2.23
$\overline{\langle v\rangle'^2}/u_*^2$ at $z/h_c = 2$	1.77	1.83	1.83	1.99
$\overline{w'^2}/u_*^2$ at $z/h_c = 2$	1.85	1.85	1.76	1.75
$\overline{\langle w\rangle'^2}/u_*^2$ at $z/h_c = 2$	1.46	1.58	1.52	1.50

3 Results

Evaluations of the Reynolds stress budgets using LESs (Andrén and Moeng 1993; Moeng and Sullivan 1994; Heinze et al. 2015) and higher-order closure models (Donaldson 1973; Mellor 1973; Mellor and Yamada 1974, 1982; Sun and Ogura 1980) of the ABLs have been presented in the (X, Y, Z) coordinate. Most of their counterparts in the surface layer, including the RSL (Wilson and Shaw 1977; Shaw and Seginer 1985; Meyers and Paw U 1986; Wilson 1988; Leclerc et al. 1990; Meyers and Baldocchi 1991; Katul and Albertson 1998) have adopted the streamline coordinate (x, y, z) which is often defined by the mean wind at the canopy top with $z = Z$ over flat terrain. This is because of the need to compare model results with field observations or wind-tunnel experiments. In Table 1, the horizontal mean wind velocities at the canopy top in the (x, y, z) coordinate are denoted by $\left(\overline{\langle u\rangle}_{h_c}, \overline{\langle v\rangle}_{h_c}\right)$ in which $\overline{\langle v\rangle}_{h_c} = 0$. Although Ayotte et al. (1999) presented the governing equations of a second-order closure model for neutrally stratified vegetative canopy flows in the (X, Y, Z) coordinate, all simulations were shown in rotated coordinates so that the mean flow is in the x-direction. Both the Coriolis force and the external pressure-gradient force were neglected in that study. An exception is the simplified second moment closure model for turbulent airflow in and above a forest (Yamada 1982), which was applied in the (X, Y, Z) coordinate. The two coordinates differ when horizontal mean wind direction changes with altitude, which is the case in shear-driven ABLs in barotropic atmosphere (Andrén and Moeng 1993; Moeng and Sullivan 1994; Lin et al. 1997; Berg et al. 2020). Below we compare profiles of horizontal mean wind velocities, Reynolds stress containing horizontal velocities and their budgets between these two coordinates for the 4 large-domain LES cases (Table 1). Any parametrization schemes, including those for pressure redistribution we evaluate in a companion paper, should be applicable to both coordinates. The (x, y, z) coordinate results from rotating the (X, Y, Z) coordinate in the X-Y plane by the angle α_{h_c} which is the horizontal mean wind directional angle counter-clockwise from the east at the canopy top (Table 1). Also calculated at the canopy top are the turbulent shear length scale $L_s = \overline{\langle u\rangle}_{h_c} / \left(\partial\overline{\langle u\rangle}/\partial z\right)_{h_c}$ in which $\left(\partial\overline{\langle u\rangle}/\partial z\right)_{h_c}$ is the mean wind shear (Raupach et al. 1996), the friction velocity $u_* = \left\{\left(\overline{\langle u\rangle'\langle w\rangle'} + \bar{\tau}_{xz}\right)^2 + \left(\overline{\langle v\rangle'\langle w\rangle'} + \bar{\tau}_{yz}\right)^2\right\}^{1/4}$

in which $\bar{\tau}_{xz}$ and $\bar{\tau}_{yz}$ are the SFS shear stresses, and the bulk drag coefficient $C_D = u_*^2 / \overline{\langle u \rangle}_{h_c}^2$. Results from the 4 earlier small-domain LES runs (Table 2) and field observation at Camp Borden, as well as their comparisons with the 4 large-domain LES cases, are presented in the (x, y, z) coordinate, in which the velocity components are denoted by (u, v, w) with $w = W$ and $\overline{\langle w \rangle} = 0$.

In addition to much smaller domains, the earlier LES Runs A–D (Table 2) are not driven by a prescribed external pressure-gradient force as typically done in an LES of shear-driven ABL (Andrén and Moeng 1993; Moeng and Sullivan 1994; Lin et al. 1997; Berg et al. 2020) and in the 4 large-domain LES Cases 1–4 in this study (Table 1). Instead, a momentum source is added at the top of the domain that equals the total moment sink imposed by the forest canopy. Because of the artifacts of this momentum source, Su et al. (1998a, 1998b) presented results up to 2 h_c. This is followed below for the results from LES Runs A and C, and up to 3 h_c for the results of LES Runs B and D (Su et al. 2000) because they have a vertical domain twice of that in Runs A and C (Table 2).

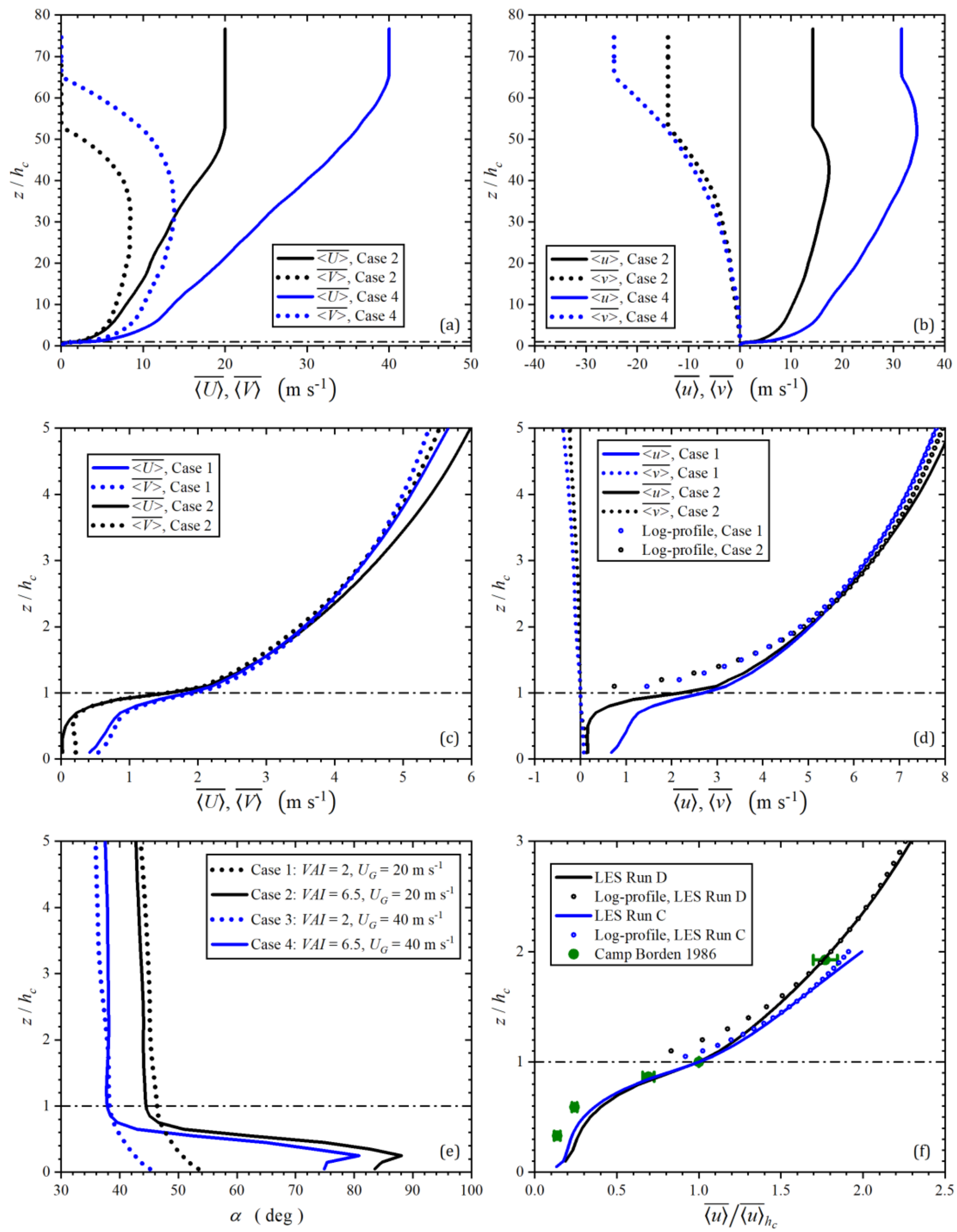

Fig. 2 Profiles of $\overline{\langle U \rangle}$ and $\overline{\langle V \rangle}$: (a) and (c); $\overline{\langle u \rangle}$ and $\overline{\langle v \rangle}$: (b) and (d); horizontal mean wind directional angle α counter-clockwise from the east: (e); normalized mean wind $\overline{\langle u \rangle}/\overline{\langle u \rangle}_{h_c}$: (f). The logarithmic mean wind profiles in (d) and (f) are calculated as $(u_*/\kappa)\ln[(z-d)/z_0]$ in which $\kappa = 0.4$ is the von Kármán constant. The values of u_*, d, and z_0 are given in Tables 1 and 2

3.1 Mean Wind

The contrast in horizontal mean wind in the east-north (X, Y) coordinate (Fig. 2a) and in the streamline coordinate (x, y) defined at the canopy top (Fig. 2b) is shown for LES Cases 2 and 4. Both $\overline{\langle U\rangle}$ and $\overline{\langle V\rangle}$ (Fig. 2a) are positive throughout the ABL. In contrast, only $\overline{\langle u\rangle}$ is positive throughout the ABL, and $\overline{\langle v\rangle}$ is mostly negative in the bulk of the ABL (Fig. 2b), except inside the forest (Fig. 2d). The $\pm$ signs of the horizontal mean wind velocities and of their vertical gradients determine the $\pm$ signs of corresponding vertical momentum flux or tangential Reynolds shear stress (Fig. 3c, d) and their shear production (Fig. 6). Similar to Moeng and Sullivan (1994), the profiles of $\overline{\langle U\rangle}$ and $\left(\overline{\langle U\rangle}^2 + \overline{\langle V\rangle}^2\right)^{1/2}$ (not shown) in the present study (Fig. 2a) do not show the supergeostrophic jet near the top of the ABL that has been shown in other LESs of inversion-capped neutral ABLs (Lin et al. 1997; Pedersen et al. 2014; Salesky et al. 2017; Berg et al. 2020). A number of factors could contribute to this and other differences in the mean wind profiles among these studies. First, the RSL in and above the forest canopies are explicitly resolved and the moment sink (form drag) is distributed throughout the 20 m tall forests in the present study. In contrast, the RSL is not explicitly resolved (including the case with $z_0 = 0.83$ m representing urban centres in Lin et al. 1997). The main momentum sink is SFS stress parametrized with wind at the first grid from the surface with roughness lengths that varied among different studies (0.01 m in Pedersen et al. 2014; 0.05 m in Berg et al. 2020; 0.10 m in Salesky et al. 2017; 0.018 m to 0.83 m in Lin et al. 1997). Patton et al. (2003) illustrated differences in mean wind profiles with and without a plant canopy in a convective boundary layer. Other factors that also varied among these studies include: (1) the geostrophic wind speed or external horizontal pressure gradient force; (2) the ABL depth; (3) the inversion strength in the free atmosphere above the ABL (Pedersen et al. 2014); and (4) the grid resolution which is important both near the surface and in the capping inversion layer or interfacial layer between the well-mixed layer below and the stable free atmosphere above (Berg et al. 2020). Lin et al. (1997) reported that the supergeostrophic jet is reduced in both speed and the vertical extent when the surface roughness length increases. In comparison, the roughness length is more than three times greater ($z_0 = 2.6 - 3$ m) in our simulations (Table 1) than the largest value in Lin et al. (1997).

Focusing on the surface layer below 5 h_c, $\overline{\langle U\rangle}$ and $\overline{\langle V\rangle}$ are comparable in magnitude in and above both the sparse (LES Case 1) and the dense (LES Case 2) model forests, except in the lower half of the dense forest where $\overline{\langle U\rangle}$ is negligible compared to $\overline{\langle V\rangle}$ (Fig. 2c). This is because turbulent transport of horizontal momentum is much reduced in the lower half of the dense forest (Fig. 3c), and $\overline{\langle V\rangle}$ is largely maintained by the external pressure-gradient force in the *Y*-direction. In contrast, $\overline{\langle v\rangle}$ is mostly negligible compared to $\overline{\langle u\rangle}$, except in the lower part of the dense forest where $\overline{\langle u\rangle}$ is comparable to $\overline{\langle v\rangle}$ (Fig. 2d), both of which are largely vector components of $\overline{\langle V\rangle}$. The horizontal mean wind directions changed little with altitude above the canopy and do not differ significantly between the two model forests for the same external horizontal pressure-gradient force (Fig. 2e), which is in agreement with Lin et al. (1997) in the surface layer over both smooth and rough surfaces. However, the horizontal mean winds illustrate increased counter-clockwise rotation with increased depth into the forest, and this wind directional shear is much stronger in the dense model forest as $\overline{\langle U\rangle}$ is more rapidly diminished with increased depth into the forest (Fig. 2c). Significant wind directional shear has also been observed in an old-growth temperate rainforest (Pyles et al. 2004). A stronger external pressure-gradient force or equivalent geostrophic wind (LES Cases 3 and 4) yielded a smaller horizontal wind direction angle α, including α_{h_c} at the canopy top, by 6^o–8^o (Table 1). The values of α in the surface layer of the shear ABL (Moeng and Sullivan 1994) are another 5^o–8^o smaller. As a result, the magnitudes of $\overline{\langle V\rangle}$, $\overline{\langle V\rangle'^2}$ and $\overline{\langle V\rangle'\langle W\rangle'}$ are more different (smaller) than $\overline{\langle U\rangle}$, $\overline{\langle U\rangle'^2}$ and $\overline{\langle U\rangle'\langle W\rangle'}$ in Moeng and Sullivan (1994), and in LES Cases 3 and 4, than in LES Cases 1 and 2. There is little horizontal mean wind directional shear in the earlier LES Runs A–D (Table 2) both above and inside the sparse model forest. This is because both the Coriolis force and the external pressure-gradient force are neglected, and the horizontal mean wind is maintained by downward turbulent transport of momentum, which is not diminished to negligible level in the lower half of the sparse model forest (Fig. 4d).

The logarithmic layer is identified by matching $\overline{\langle u\rangle}$ and $(u_*/\kappa)\ln[(z-d)/z_0]$ with the differences between them less than 0.01 m s^{-1}, where $\kappa = 0.4$ is the von Kármán constant. The zero-plane displacement height d is calculated as the mean level of momentum absorption $d = \int_0^{h_c} z\left(\mathrm{d}\overline{u'w'}/\mathrm{d}z\right)\mathrm{d}z \Big/ \int_0^{h_c}\left(\mathrm{d}\overline{u'w'}/\mathrm{d}z\right)\mathrm{d}z$ (Thom 1971; Jackson 1981; Brunet et al. 1994; Su et al. 1998a; Nepf and Vivoni 2000). For the LESs in this study, we have $\overline{u'w'} = \overline{\langle u\rangle'\langle w\rangle'} + \bar{\tau}_{xz}$ and $\overline{v'w'} = \overline{\langle v\rangle'\langle w\rangle'} + \bar{\tau}_{yz}$. The impact of $\overline{v'w'}$ is negligible since it is much less than $\overline{u'w'}$ in the upper portions of the canopy (Fig. 3d) where the momentum absorption has the dominant impact on estimated d. This method for estimating d does not depend on mean wind or momentum flux in either RSL or ISL above the canopy. Therefore, it does not have to resort to an empirical function to account for the impact of RSL on the flux-gradient relation for moment derived for the ISL above the canopy as was the case in Weligepolage et al. (2012). The roughness length z_0 is then found by fitting the logarithmic mean wind profile $(u_*/\kappa)\ln[(z-d)/z_0]$ to $\overline{\langle u\rangle}$ from the LES in a layer above the forest where $\overline{\langle u\rangle}$ is a linear function of $\ln(z-d)$ (Su et al. 1998a). The difference in identified logarithmic layer is negligible when $\left(\overline{\langle u\rangle}^2 + \overline{\langle v\rangle}^2\right)^{1/2}$ instead of $\overline{\langle u\rangle}$ is used because $\overline{\langle v\rangle} \ll \overline{\langle u\rangle}$ in the surface layer above the canopy (Fig. 2d). Below the logarithmic layer is the RSL (Kaimal and Finnigan 1994). In the above canopy portion of the RSL, the horizontal mean wind is stronger than that specified by corresponding logarithmic profile hence a weaker mean wind shear (Fig. 2d, f) due to stronger turbulence mixing or enhanced eddy diffusivity (Raupach et al. 1986; Garratt 1992; Brunet et al. 1994; Su et al. 1998a).

The depths of both the RSL and the logarithmic layer are the smallest in LES Runs A and C, which have the smallest vertical domain, and the depths increased with increased LES domain (Tables 1 and 2). All 4 earlier small-domain LES runs (Table 2, Fig. 2f) yielded the RSL depths less than the typical range of $2-3\,h_c$, which however, are produced by the 4 large-domain LES cases (Table 1, Fig. 2d). The smallest domain in LES Run C yielded a stronger vertical shear of horizontal mean wind between 1.4 h_c and 2 h_c, than LES Run D, and the latter better matched observed mean wind at about 2 h_c (Fig. 2f). This contributes to difference in shear production of Reynolds stress in the same region between LES Runs C and D discussed later (Fig. 9a, b). As expected and shown in previous LES work (Shaw and Schumann 1992; Dupont and Brunet 2008b), the dense forest (LES Case 2) yielded a much stronger vertical shear of horizontal mean wind than the sparse forest (LES Case 1) near the canopy top (Fig. 2c, d). The turbulent shear length scale L_s

(Table 1) for the dense forest (LES Cases 2 and 4) is less than half of that for the sparse forest (LES Cases 1 and 3). The values of L_s for the earlier small-domain LES Runs A, B, and D (Table 2) are about twice that in LES Cases 1 and 3 due to smaller vegetation density in the upper portions of the canopy despite of the same *LAI* or *VAI* value of 2. A reduced grid spacing in LES Run C led to a smaller L_s and stronger shear at the canopy top. It should be noted that the RSL is not explicitly simulated in the LESs of shear ABLs (Andrén and Moeng 1993; Moeng and Sullivan 1994; Lin et al. 1997; Berg et al. 2020), including over a rough surface representing the centre of large towns and cities with $z_0 = 0.83$ m (Lin et al. 1997), which is less than 1/3 of the values in this study (Tables 1, 2). It is not clear if or how the zero-plane displacement height d is represented over this rough surface because the vertical grid spacing of 7.5 m (Lin et al. 1997) could be less than d over urban canopies in the centre of large towns and cities. Despite of this, Lin et al. (1997) reported mean winds in the surface layers being linear functions of $\ln(z/z_0)$ with different roughness values: smooth $(z_0 = 0.018\ \mathrm{m})$, rough $(z_0 = 0.83\ \mathrm{m})$, and intermediate $(z_0 = 0.16\ \mathrm{m})$. However, the mean wind profiles from their LESs are not directly compared with the logarithmic profile as we have done here (Fig. 2d, f). Andrén and Moeng (1993) failed to produce the logarithmic wind profile in the surface layer, which could be due to a coarser grid resolution (30 m in the vertical direction) and deficiencies in the SFS stress modelling. Unlike Andrén and Moeng (1993), Lin et al. (1997) adopted the two-part SFS eddy-viscosity model (Sullivan et al. 1994) which has been shown to improve in producing the logarithmic mean wind profiles in the surface layer.

The ABL height z_i for the 4 large-domain LES Cases 1–4 (Table 1) is determined by the height of maximum $\partial\overline{\langle\theta\rangle}/\partial z$ following Sullivan et al. (1998) since it is consistent with flow visualization and representative of entrainment interface. This is also adopted in Patton et al. (2016) and Berg et al. (2020). At these values of z_i, the friction velocities are reduced to 0.2–0.6% of respective maximum values at the canopy top, and $\overline{\langle V\rangle}$ are close to zero as the mean winds approach geostrophic (Fig. 2a). These values of z_i are greater by 35–43% (LES Cases 1 and 2) and 55–75% (LES Cases 3 and 4) than those (values of z_i in the parentheses in Table 1) determined by the minimum (peak negative) heat flux, which is used in Moeng and Sullivan (1994), Lin et al. (1997), Pedersen et al. (2014), Salesky et al. (2017), and Banerjee et al. (2017), but has been shown to be more variable in time

(Sullivan et al. 1998). These differences are further discussed in Appendix 1. The values of z_i determined by maximum $\partial\overline{\langle\theta\rangle}/\partial z$ are also greater than those when the friction velocity is reduced to 10% of its maximum value at the surface (Andrén and Moeng 1993), which is at the canopy top in the present study (Table 1). Despite these differences, the ratio z_i/h_c in LES Cases 1–4 are much greater (at least 36 h_c) than earlier LESs of airflows in and above plant canopies (Shaw and Schumann 1992; Dwyer et al. 1997; Shen and Leclerc 1997; Su et al. 1998a, 2000; Dupont and Brunet 2008b; Finnigan et al. 2009) and wind-tunnel experiment (Raupach et al. 1986; Brunet et al. 1994; Shaw et al. 1995). The values of z_i in our four large-domain LES cases are also greater than those in the other larger-domain high-resolution canopy-resolving LESs (Patton et al. 2016; Banerjee et al. 2017) or larger-domain LESs of inversion-capped neutral ABLs over smoother surfaces (Pedersen et al. 2014; Berg et al. 2020). This indicates that the much larger horizontal domains in these studies do not necessarily lead to greater ABL depths. Finally, these values of z_i allow comparisons to be made among studies in which different length scales (z_i or h_c) are used in normalizing Reynolds stress and their budgets in the surface layer comprised of the RSL and the ISL. An example is comparing energy spectra at different normalized heights among different studies (Fig. 13f and Fig. 14f) in Appendix 1.

3.2 Reynolds Stress

The contrast in normalized horizontal velocity variances in the (X, Y) coordinate (Fig. 3a) and in the (x, y) coordinate (Fig. 3b) between LES Case 1 ($VAI = 2$) and Case 2 ($VAI = 6.5$) is shown in the surface layer below 5 h_c. Similar to the mean wind velocities (Fig. 2c), $\overline{\langle U\rangle'^2}$ and $\overline{\langle V\rangle'^2}$ also have comparable magnitudes (Fig. 3a), including in the lower half of the dense forest where a difference is that $\overline{\langle U\rangle}$ is negligible compared to $\overline{\langle V\rangle}$ (Fig. 2c). Similar to the field observations (Shaw et al. 1988), $\overline{\langle u\rangle'^2}$ is significantly greater than $\overline{\langle v\rangle'^2}$ above both model forests and in the top 1/3 of the canopy where both $\overline{\langle u\rangle'^2}$ and $\overline{\langle v\rangle'^2}$ decreased with increased depth into the canopy more rapidly in the denser model forest (Fig. 3b). These decreases are also more rapid in $\overline{\langle u\rangle'^2}$ than in $\overline{\langle v\rangle'^2}$ such that $\overline{\langle u\rangle'^2}$ is less than $\overline{\langle v\rangle'^2}$ in the lower half of the sparse ($VAI = 2$) forest, which has also been observed in a partially defoliated ($LAI = 1.6$) forest (Shaw et al. 1988), and shown in the LES of Patton et al. (2016) in and above a deciduous walnut orchard (one-sided plant area index $PAI = 2$) in near-neutral stratification. In the lower half (trunk space) of both model forests, the values of $\overline{\langle U\rangle'^2}$, $\overline{\langle V\rangle'^2}$, $\overline{\langle u\rangle'^2}$ and $\overline{\langle v\rangle'^2}$ are very close to each other and vary little with height. Their normalized (by u_*^2) values are ~ 0.2 in the dense forest, and 0.3–0.4 in the sparse forest (Fig. 3b) and in Patton et al. (2016) after we changed the velocity scale used for normalization in Patton et al. (2016) to u_* for their near-neutral (NN) case. This feature is attributed to the dominant sources of horizontal velocity variances being pressure redistribution in this region as discussed later (Fig. 5a–d, Fig. 8a, b).

Similarly, the magnitudes of $\overline{\langle U\rangle'\langle W\rangle'}$ and $\overline{\langle V\rangle'\langle W\rangle'}$ are comparable (Fig. 3c), but the magnitude of $\overline{\langle v\rangle'\langle w\rangle'}$ is much smaller than that of $\overline{\langle u\rangle'\langle w\rangle'}$ (Fig. 3d), except in the lower half of the dense forest where $\overline{\langle u\rangle'\langle w\rangle'}$, as well as $\overline{\langle U\rangle'\langle W\rangle'}$ and $\overline{\langle V\rangle'\langle W\rangle'}$, are also negligible. In addition, $\overline{\langle v\rangle'\langle w\rangle'}$ is positive in the surface layer in and above both model forests (Fig. 3d). This is also the case for $\overline{v'w'} = \overline{\langle v\rangle'\langle w\rangle'} + \bar{\tau}_{yz}$ (not shown) in which $\bar{\tau}_{yz}$ is the SFS stress. In comparison, $\overline{\langle u\rangle'\langle w\rangle'}$, as well as $\overline{\langle U\rangle'\langle W\rangle'}$ and $\overline{\langle V\rangle'\langle W\rangle'}$ are all negative, except in the lower half of the dense forest where negligible but positive values of $\overline{\langle V\rangle'\langle W\rangle'}$ are shown (Fig. 3c). For the sake of clarity, we only show $\overline{u'w'} = \overline{\langle u\rangle'\langle w\rangle'} + \bar{\tau}_{xz}$ and the SFS shear stress $\bar{\tau}_{xz}$ in Fig. 3d for LES Case 2 for the dense model forest ($VAI = 6.5$). As expected, the SFS stress $\bar{\tau}_{xz}$ peaks at the treetops and accounts for 18% of the total stress $\overline{u'w'}$. In addition to SFS stresses $\bar{S}_{xx} = \bar{\tau}_{xx} + 2\overline{\langle e\rangle}/3$ (Fig. 3b) and $\bar{\tau}_{xz}$ (Fig. 3d) shown for the surface layer, full ABL profiles of $\overline{\langle e\rangle}$, $\bar{\tau}_{xz}$ and SFS heat flux $\bar{\tau}_{\theta z}$ are given in Appendix 1 (Fig. 11).

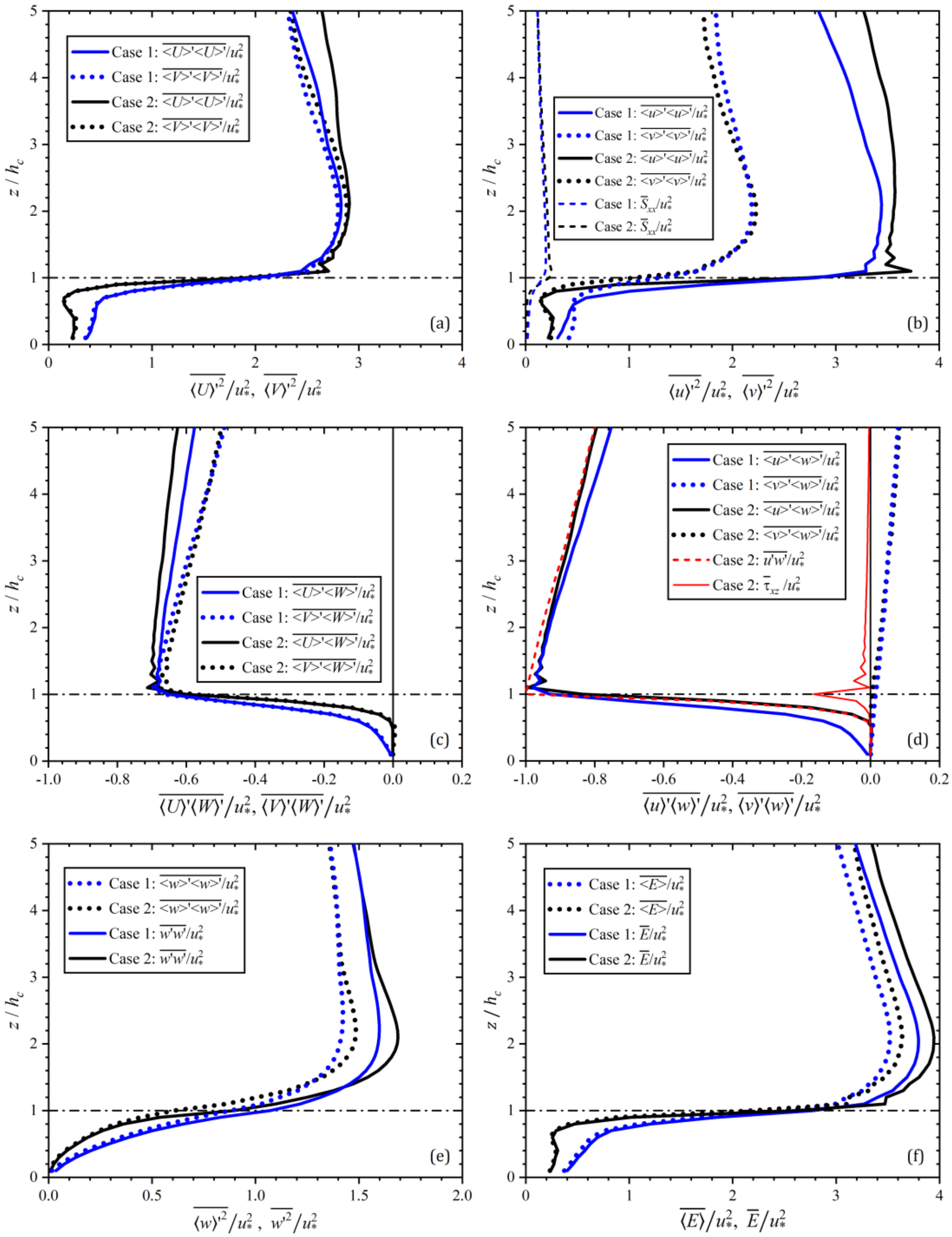

Fig. 3 Profiles of (a) $\overline{\langle U\rangle'^2}/u_*^2$ and $\overline{\langle V\rangle'^2}/u_*^2$; (b) $\overline{\langle u\rangle'^2}/u_*^2$, $\overline{\langle v\rangle'^2}/u_*^2$, and $\bar{S}_{xx}/u_*^2$ in which $\bar{S}_{xx} = \bar{\tau}_{xx} + 2\overline{\langle e\rangle}/3$; (c) $\overline{\langle U\rangle'\langle W\rangle'}/u_*^2$ and $\overline{\langle V\rangle'\langle W\rangle'}/u_*^2$; (d) $\overline{\langle u\rangle'\langle w\rangle'}/u_*^2$, $\overline{\langle v\rangle'\langle w\rangle'}/u_*^2$, $\bar{\tau}_{xz}/u_*^2$, and $\overline{u'w'}/u_*^2$ where $\overline{u'w'} = \overline{\langle u\rangle'\langle w\rangle'} + \bar{\tau}_{xz}$; (e) $\overline{\langle w\rangle'^2}/u_*^2$ and $\overline{w'^2}/u_*^2$ where $\overline{w'^2} = \overline{\langle w\rangle'^2} + \bar{\tau}_{zz} + 2\overline{\langle e\rangle}/3$; (f) $\overline{\langle E\rangle}/u_*^2$ and $\bar{E}/u_*^2$ where $\bar{E} = \overline{\langle E\rangle} + \overline{\langle e\rangle}$; for LES Cases 1 and 2

The SFS contributions can be seen as differences between the total and the resolved-scale vertical velocity variance (Fig. 3e), TKE (Fig. 3f), and all three velocity variances at $z/h_c = 1$ and 2 (Tables 1, 2). In the surface layer above the canopy, SFS stress account for 8–18% of total vertical velocity variance (Fig. 3e), and SFS kinetic energy account for 5–10% of total TKE (Fig. 3f). The SFS stress counts for a smaller percentage of the total horizontal velocity variance. This is because the resolved-scale velocity variances are greater in the horizontal directions (Fig. 3b) than in the vertical direction (Fig. 3e) while differences among SFS normal stress components are negligible. The percentages of SFS normal stress peaks at the canopy top, 18% and 32% of total vertical velocity variance (Tables 1 and 2) for the sparse and dense model forest, respectively. It should be noted that unlike in the 4 earlier small-domain LES Runs A–D (Table 2), the wake energy is not included in the 4 large-domain LES Cases 1–4 (Table 1), which could have the same magnitudes as the SFS kinetic energy inside the forests. However, contributions by wake turbulence to SFS momentum fluxes are small due to their small length scales (Shaw and Patton 2003).

Comparisons of Reynolds stress containing horizontal velocities in the surface layer among different LESs of shear ABLs and with field observation or wind-tunnel experiment should be made in the (x, y, z) coordinate. A number of factors such as surface roughness (Lin et al. 1997), geostrophic wind speed and ABL depth (Table 1) influence the horizontal mean wind direction (α) in the surface layer (Fig. 2e), including α_{h_c} at the canopy top that is used to define the (x, y, z) coordinate. This leads to differences in the relative magnitudes between $\overline{\langle U \rangle}$ and $\overline{\langle V \rangle}$, between $\overline{\langle U \rangle'^2}$ and $\overline{\langle V \rangle'^2}$, and between $\overline{\langle U \rangle'\langle W \rangle'}$ and $\overline{\langle V \rangle'\langle W \rangle'}$ among different LES studies that render it difficult to compare them. The Reynolds stress and related budgets in the LESs of shear ABLs (Andrén and Moeng 1993; Moeng and Sullivan 1994; Lin et al. 1997) are presented in the (X, Y, Z) coordinate. However, Andrén and Moeng (1993) appears to have compared normalized Reynolds stress in the (X, Y, Z) coordinate with field observation in the (x, y, z) coordinate in the surface layer over smooth surfaces. Below we compare Reynolds stress and related budgets from the 4 large-domain LES cases (Table 1) and the 4 earlier small-domain LES runs (Table 2) and field observation in the (x, y, z) coordinate.

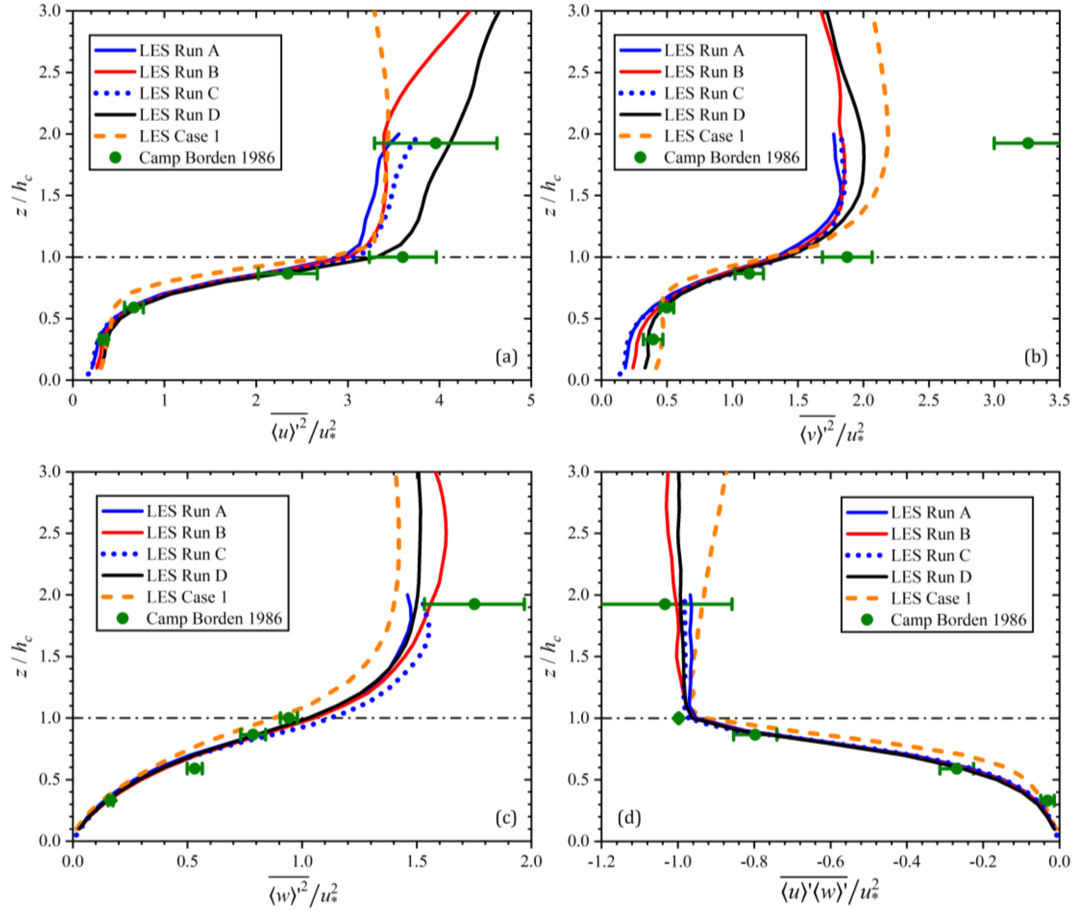

Fig. 4 Profiles of normalized Reynolds stress among LES Runs A−D and LES Case 1 with different domain size or grid spacing and field observation: (a) $\overline{\langle u\rangle'^2}/u_*^2$; (b) $\overline{\langle v\rangle'^2}/u_*^2$; (c) $\overline{\langle w\rangle'^2}/u_*^2$; (d) $\overline{\langle u\rangle'\langle w\rangle'}/u_*^2$. The field observation at Camp Borden is based on time average of observed turbulent scales, whereas the LES results are for the resolved-scale flow field only

The same field observation presented in Su et al. (1998a) are used to compare with the 4 earlier LES Runs A−D (Table 2) to examine the effects of domain size and grid spacing (Fig. 4). Unlike Su et al. (1998a) in which standard deviations of velocities are shown, here velocity variances are presented. As expected, a finer grid spacing in Run C, which has the same domain size as Run A, led to greater resolved-scale Reynolds stress, particularly in the upper 1/3 of the forest and above the canopy. Doubling the horizontal domain (Run D) led to greater increases in resolved-scale velocity variances in the horizontal directions than doubling the vertical domain only in Run B (Fig. 4a, b). Reducing the grid spacing by half

(Run C) led to a greater increase in $\overline{\langle w\rangle'^2}/u_*^2$ (Fig. 4c) than doubling the domain in both horizontal and vertical directions (Run D), whereas the opposite is shown in $\overline{\langle u\rangle'^2}/u_*^2$ (Fig. 4a) and $\overline{\langle v\rangle'^2}/u_*^2$ (Fig. 4b). The impacts of reducing the grid spacing by half and of doubling the domain on $\overline{\langle u\rangle'\langle w\rangle'}/u_*^2$ are comparable above the canopy and negligible inside the forests (Fig. 4d). One interesting result is in the lower half of the canopy where horizontal velocity variances increased with increased domain, including the large-domain LES Case 1 (Fig. 4a, b). As discussed earlier (Fig. 3a, b), the dominant source of horizontal velocity fluctuations in this region is pressure-redistribution, which is shown later to increase with increased LES domain (Fig. 10a, b).

LES Case 1 is included to examine the effects of an even larger LES domain than LES Run D. However, it has a different vertical distribution of a_p although the same *VAI* of 2 as LES Runs A–D. The decrease in normalized Reynolds stress with increased depth into the forest is more rapid in LES Case 1 than in LES Runs A–D because of greater a_p in the upper portions of the canopy in LES Case 1 (Fig. 1). However, the effect of a much larger domain in LES Case 1 than LES Run D varied among different Reynolds stress components above the canopy. For example, LES Run D yielded greater magnitudes of $\overline{\langle u\rangle'^2}/u_*^2$, $\overline{\langle w\rangle'^2}/u_*^2$ and $\overline{\langle u\rangle'\langle w\rangle'}/u_*^2$, but smaller $\overline{\langle v\rangle'^2}/u_*^2$ than LES Case 1.

The impacts of LES domain size and grid spacing discussed above point to one possible factor (i.e., differences in the ranges of turbulent length scales normalized by canopy height) contributing to the differences between the LESs and the field observation in and above a sparse forest at Camp Borden. Other factors such as plant morphology may also contribute to the differences in the "family portrait" of canopy turbulence, including profiles of normalized standard deviations of velocities in the horizontal mean wind and vertical directions (Raupach et al. 1996; Finnigan 2000). Overall, the agreements between LES Runs A–D and field observations are better inside the forests than above the forest, and better in $\overline{u'^2}/u_*^2$ and $\overline{w'^2}/u_*^2$ than in $\overline{v'^2}/u_*^2$ above the canopy. Although only the resolved-scale velocity variances are shown in Fig. 4a–c, both the resolved-scale and total velocity variances at $z/h_c = 1$ and 2 are provided in Table 2 for LES Runs A–D and in Table 1 for LES Cases 1–4. Raupach et al. (1996) stated that well above the canopy

($z/h_c > 2$), the flow assumes the ISL, and typical values of $\overline{u'^2}/u_*^2$ and $\overline{w'^2}/u_*^2$ are 6.25 and 1.56, respectively (Garratt 1992). Most field observations over tall forests (Shaw et al. 1988; Meyers and Baldocchi 1991; Gardiner 1994; Katul and Alberston 1998), however, do not extend much beyond $z/h_c > 2$, therefore are most likely in the RSL. This is also the case in the "family portrait" of single-point statistics (Raupach et al. 1996; Finnigan 2000) which are only up to $z/h_c = 2$. In the Canopy Horizontal Array Turbulence Study (CHATS) experiment (Patton et al. 2011), seven 3-D sonic anemometer-thermometers (Campbell Scientific CSAT3) were installed between the canopy top and the highest level of only 2.9 h_c.

A consistent feature among the LESs and the field observation is that normalized velocity variances in the RSL above canopy decrease from about twice the canopy height towards the canopy top, and such decreases are more rapid in the crosswind and vertical directions than in the mean wind direction (Fig. 4, Tables 1, 2). These decreases are also shown in $\overline{u'^2}/u_*^2$ and $\overline{w'^2}/u_*^2$ from $z/h_c = 1.9$ to 1 over a very dense ($LAI = 10.2$) Sitka spruce forest (Gardiner 1994) and from $z/h_c = 1.4$ to 1 over a loblolly pine stand with *LAI* of 3.82 (Katul and Alberston 1998), and in $\overline{u'^2}/u_*^2$ and $\overline{v'^2}/u_*^2$ from $z/h_c = 1.2$ to 1 over a fully leafed ($LAI = 5$) eastern hardwood oak-hickory forest (Meyers and Baldocchi 1991). From the CHATS experiment, Patton et al. (2011) showed similar decreases in vertical velocity standard deviations (not normalized) from peaks at heights from 1.4 h_c to 2.9 h_c that varied with time of the day (so likely stability) to the canopy top. These decreases are also less in the streamwise velocity standard deviations than in the vertical velocity standard deviation (Dupont and Patton 2012), which are normalized by the mean wind speed measured at the canopy top instead of friction velocity.

Another agreement between the 4 large-domain LES cases (Fig. 3b, e and Table 1) and field observation over a deciduous forest (Shaw et al. 1988) is that $\overline{u'^2}/u_*^2$ and $\overline{w'^2}/u_*^2$ in the RSL above the canopy increased with increased *VAI* (from 2 to 6.5 in this study) or *LAI* (from 1.6 to 4.9 in the field observation of Shaw et al. 1988) by a similar amount, ~ 0.2 in $\overline{u'^2}/u_*^2$ and ~ 0.1 in $\overline{w'^2}/u_*^2$.

However, less consistent are the maximum values of normalized velocity variances in the RSL above the canopy among the LES results and field observations over various forests cited above, and more variable in the horizontal mean wind direction than in the vertical direction. For example, at $z/h_c = 2$, the maximum value in $\overline{u'^2}/u_*^2$ from the LESs is ~ 4.25 over the dense model forest (Table 1), far less than 6.25 observed in the surface layer over smooth surfaces. This is also the case in field observation over a partially defoliated ($LAI = 1.6$) forest (Fig. 4a). However, Shaw et al. (1988) showed that $\overline{u'^2}/u_*^2$ reached 6.25 at $z/h_c = 1.9 - 2.4$ when the deciduous forest at Camp Borden was fully foliated ($LAI = 4.9$), and the same value was observed at $z/h_c = 1.4$ over a loblolly pine stand with an LAI of 3.82 (Katul and Alberston 1998). Earlier observations in the surface layer over a flat smooth surface (Panofsky 1973) reported $\overline{v'^2}/u_*^2 = 4.84$ with a very large range from 9 to 2.25. The field observations above a 15 m tall very dense ($LAI = 10.2$) Sitka spruce forest (Gardiner 1994) also reported large ranges in normalized streamwise and vertical velocity variance: at $z/h_c = 1$, $\overline{u'^2}/u_*^2 = 4 - 6$, $\overline{w'^2}/u_*^2 = 1.2 - 2.6$; and at $z/h_c = 1.9$, $\overline{u'^2}/u_*^2 = 4.8 - 10.2$, $\overline{w'^2}/u_*^2 = 1.2 - 3.6$. As pointed out by Panosfky (1973) and is well known now, mesoscale processes may contribute significantly to horizontal velocity variances measured in the field. Therefore, data processing such as detrending or filtering could have a large impact on reported values of $\overline{u'^2}/u_*^2$ and $\overline{v'^2}/u_*^2$. This is usually not an issue in the LESs of ABLs including the present work or in wind-tunnel experiment (Raupach et al. 1986; Brunet et al. 1994; Yue et al. 2008). Brunet et al. (1994) reported $\overline{u'^2}/u_*^2 = 4$ and $\overline{w'^2}/u_*^2 = 1.21$ at the top of a 47 mm tall artificial wheat canopy ("leaf" area index $LAI = 0.47$); and $\overline{u'^2}/u_*^2 = 4.84$ and $\overline{w'^2}/u_*^2 = 1.69$ in the constant stress layer up to $z/h_c = 2$. These values are fairly close to our LES results (Tables 1 and 2). Therefore, the normalized velocity variances observed in the atmospheric surface layer over flat smooth surfaces (Panofsky 1973; Garratt 1992): $\overline{u'^2}/u_*^2 = 6.25$, $\overline{v'^2}/u_*^2 = 4.84$, $\overline{w'^2}/u_*^2 = 1.56 - 1.69$, may not be as useful as the logarithmic mean wind profile or negligible turbulent transport in Reynolds stress budgets discussed later in Sect. 3.3, in determining if the ISL exists over tall forests.

For various reasons (sensor limitation or by choice), the values of normalized crosswind velocity variance $\overline{v'^2}/u_*^2$ in the RSL have rarely been reported in the literature.

This is the case not only in field observations (Gardiner 1994; Patton et al. 2011; Dupont and Patton 2012), including those used to compare with higher-order closure model results (Wilson and Shaw 1977; Meyers and Paw U 1986; Wilson 1988; Katul and Alberston 1998; Ayotte et al. 1999), and wind-tunnel experiments (Raupach et al. 1986; Brunet et al. 1994), but also in some LESs of airflows in and above plant canopies (Shen and Leclerc 1997; Yue et al. 2007; Banerjee et al. 2017). One exception in field observation is Shaw et al. (1988), and the other is Meyers and Baldocchi (1991). In the latter, the Reynolds stress is normalized by friction velocity measured above the forest at $1.2h_c$ which is shown to be significantly smaller than that measured at the canopy top (Baldocchi and Meyers 1988). The friction velocity calculated at the canopy top is typically used for normalization.

Finally, the kinks in the profiles of $\overline{\langle U\rangle'^2}$ (Fig. 3a), $\overline{\langle u\rangle'^2}$ (Fig. 3b), $\overline{\langle U\rangle'\langle W\rangle'}$ (Fig. 3c) and $\overline{\langle u\rangle'\langle w\rangle'}$ (Fig. 3d) just above the treetops are nonphysical. These kinks are more prominent over the dense model forest (Case 2) than the sparse forest (Case 1), and are absent in our earlier small-domain LES Runs A–D (Fig. 4). These kinks are also absent in Patton et al. (2016) over a sparse deciduous walnut orchard ($PAI = 2$), but are quite prominent in Dupont and Brunet (2008) and also visible in Banerjee et al. (2017) with PAI of 5. A possible explanation could be whether the grid resolution is adequate in resolving eddies near the canopy top, whose length scale may be represented by the turbulent shear length scale L_s, or the vorticity thickness $\delta_\omega = 2L_s$. For the near-neutral (NN) case in Patton et al. (2016), $\delta_\omega = 1.225\ h_c$ and $h_c = 20$ m, the grid spacing is an order of magnitude smaller than δ_ω, $0.125\ h_c$ in the horizontal and $0.1\ h_c$ in the vertical. In our earlier small-domain LES Runs A, B, and D with $(2\text{ m})^3$ grids, $\delta_\omega = 1.28 - 1.4\ h_c$ and $h_c = 20$ m with an LAI of 2 (Fig. 1 and Table 2), the grid spacing $0.1\ h_c$ is also an order of magnitude smaller than δ_ω. In LES Cases 1 and 3 ($VAI = 2$), $\delta_\omega = 0.66\ h_c$ and $h_c = 20$ m, but in LES Cases 2 and 4 ($VAI = 6.5$), $\delta_\omega = 0.3\ h_c$ (Table 1), for which the $0.1\ h_c$ grid spacing is likely inadequate. Information on either L_s or δ_ω is not reported in Dupont and Brunet (2008) or in Banerjee et al. (2017). Finally, these kinks are absent in the profile of the total shear stress $\overline{u'w'} = \overline{\langle u\rangle'\langle w\rangle'} + \bar{\tau}_{xz}$ (Fig. 3d) for the dense mode forest (Case 2), which is a result of the kinks in SFS stress $\bar{\tau}_{xz}$ being in the opposite direction as the kinks in $\overline{\langle u\rangle'\langle w\rangle'}$. This is also the case for LES Cases 1, 3 and 4 (not shown).

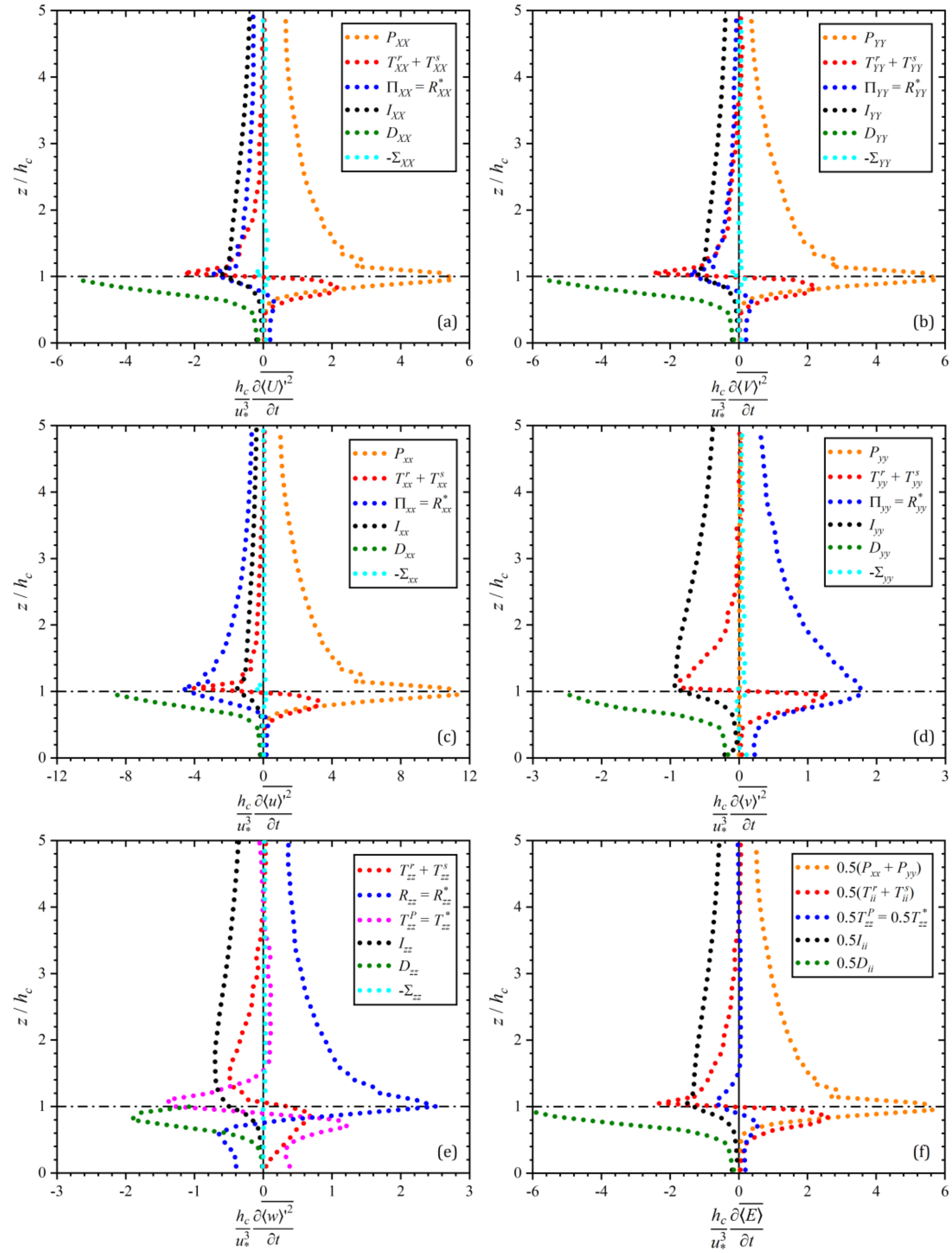

Fig. 5 A comparison of normalized budgets of the resolved-scale normal stress in the horizontal directions between two horizontal coordinates (X, Y): (a) $\overline{\langle U\rangle'^2}$; (b) $\overline{\langle V\rangle'^2}$; and ($x$, y): (c) $\overline{\langle u\rangle'^2}$; (d) $\overline{\langle v\rangle'^2}$ for LES Case 1. The normalized budgets independent of the horizontal coordinates are those of (e) $\overline{\langle w\rangle'^2}$ and (f) $\overline{\langle E\rangle}$ (resolved-scale TKE)

3.3 Budgets of Normal Stress and Turbulent Kinetic Energy

In addition to the logarithmic layer discussed in Sect. 3.1, the magnitudes of turbulent transport and pressure transport may also be used to distinguish the RSL from the ISL. In the ISL, turbulent transport and pressure transport are negligible, and shear production is balanced by dissipation (which is represented by the interscale transfer from the resolved scales to the subfilter scales in this study). The height at which turbulent transport is considered negligible depends on the criteria used, and varied among the budgets of different Reynolds stress components. For example, turbulent transport is a sink above the canopy and is reduced to less than 1% of corresponding peak sink values above the forest at $z/h_c = 3.55, 3.65, 3.75, 2.45, 3.9, 3.65$ in the budgets of $\overline{\langle U\rangle'^2}$, $\overline{\langle V\rangle'^2}$, $\overline{\langle u\rangle'^2}$, $\overline{\langle v\rangle'^2}$, $\overline{\langle w\rangle'^2}$, $\overline{\langle E\rangle}$, respectively (Fig. 5). In the RSL above the forest, pressure transport is also a sink in the budget of $\overline{\langle w\rangle'^2}$ and more significant than turbulent transport up to $z/h_c = 1.3$ (Fig. 5e). Pressure transport switches the $\pm$ sign between $z/h_c = 1.5$ and 1.6, above which it is a small and fairly constant source of $\overline{\langle w\rangle'^2}$ ($\sim 0.1\, u_*^3/h_c$) up to $z/h_c = 3.5$. Considering both turbulent transport and pressure transport are negligible in the ISL, we may use the results between $z/h_c = 4$ and $z/h_c = 5$ to represent the ISL, which is the upper part of the logarithmic layer in LES Case 1 (Table 1).

In the ISL, shear production is the only main source of $\overline{\langle U\rangle'^2}$ (Fig. 5a), $\overline{\langle V\rangle'^2}$ (Fig. 5b), $\overline{\langle u\rangle'^2}$ (Fig. 5c) or $\overline{\langle E\rangle}$ (Fig. 5f), but is negligible in the budget of $\overline{\langle v\rangle'^2}$ (Fig. 5d), and is zero in the budget of $\overline{\langle w\rangle'^2}$ (Fig. 5e). The pressure redistribution is a sink of $\overline{\langle U\rangle'^2}$, $\overline{\langle V\rangle'^2}$ or $\overline{\langle u\rangle'^2}$, but is the only major source of $\overline{\langle v\rangle'^2}$ or $\overline{\langle w\rangle'^2}$, and is zero in the budget of $\overline{\langle E\rangle}$ in an incompressible atmosphere. The interscale transfer is a sink of resolved-scale normal stress or TKE. However, it is a smaller sink than pressure redistribution in the budget of $\overline{\langle u\rangle'^2}$, and the opposite is true in the budget of $\overline{\langle U\rangle'^2}$ or $\overline{\langle V\rangle'^2}$. The pressure redistribution closely follows the shear production in the budget of $\overline{\langle U\rangle'^2}$, $\overline{\langle V\rangle'^2}$ or $\overline{\langle u\rangle'^2}$, both are the largest in the budget of $\overline{\langle u\rangle'^2}$ and the smallest in the budget of $\overline{\langle V\rangle'^2}$. This is further discussed in evaluating the parametrization of pressure redistribution in a companion paper. In contrast, the interscale transfer varied little among the budgets of $\overline{\langle U\rangle'^2}$, $\overline{\langle V\rangle'^2}$, $\overline{\langle u\rangle'^2}$ and $\overline{\langle v\rangle'^2}$. This is because unlike the interscale transfer in Perret and Patton (2021) from larger resolved scales in the ABL to smaller resolved scales near the canopy top, the interscale transfer here is from the resolved scales to the subfilter scales at which turbulence is quasi-isotropic.

In the RSL above the forest, shear production, pressure redistribution and interscale transfer are all greater than their counterparts in the ISL, and increase towards the canopy top. The increases are more rapid or greater in the sources (shear production of $\overline{\langle U\rangle'^2}$, $\overline{\langle V\rangle'^2}$ and $\overline{\langle u\rangle'^2}$, pressure redistribution of $\overline{\langle v\rangle'^2}$ and $\overline{\langle w\rangle'^2}$) than the sinks (pressure redistribution and interscale transfer of $\overline{\langle U\rangle'^2}$, $\overline{\langle V\rangle'^2}$ and $\overline{\langle u\rangle'^2}$, interscale transfer of $\overline{\langle v\rangle'^2}$ and $\overline{\langle w\rangle'^2}$). Turbulent transport is an increasingly significant sink towards the canopy top. An exception is that both interscale transfer and turbulent transport of $\overline{\langle w\rangle'^2}$ peaked at $z/h_c = 1.5$, below which pressure transport became a significant sink that increases rapidly towards the canopy top.

The RSL inside the forest is characterized in two distinct layers. In the upper half of the forest, turbulent transport is a significant source which peaks just below the canopy top. Shear production of $\overline{\langle U\rangle'^2}$, $\overline{\langle V\rangle'^2}$ and $\overline{\langle u\rangle'^2}$ and pressure redistribution of $\overline{\langle v\rangle'^2}$ and $\overline{\langle w\rangle'^2}$ continue to be the major sources, but destruction by canopy form drag is a much larger sink than pressure redistribution and interscale transfer of $\overline{\langle U\rangle'^2}$, $\overline{\langle V\rangle'^2}$ and $\overline{\langle u\rangle'^2}$, as well as interscale transfer of $\overline{\langle v\rangle'^2}$ and $\overline{\langle w\rangle'^2}$. These sources and sinks decrease rapidly with increased depth into the forest, particularly shear production and canopy form drag destruction. Pressure transport is a greater source of $\overline{\langle w\rangle'^2}$ than turbulent transport except just beneath the canopy top. In contrast, the picture appears to be much simpler in the lower half of the forest where shear production, interscale transfer and turbulent transport are much reduced, and pressure redistribution and canopy form drag destruction are the primary source and sink of normal stress in the horizontal directions ($\overline{\langle U\rangle'^2}$, $\overline{\langle V\rangle'^2}$, $\overline{\langle u\rangle'^2}$ and $\overline{\langle v\rangle'^2}$). Incompressibility ensures that pressure redistribution is the primary sink of $\overline{\langle w\rangle'^2}$, while pressure transport is the largest source. Unlike turbulent transports of the horizontal velocity variances that decrease rapidly with increased depth into the forest in the upper half of the forest to negligible levels in the lower half of the forest, turbulence transport of $\overline{\langle w \rangle'^2}$ deceases from the canopy top to the ground surface in a linear fashion, and is a smaller source than pressure transport but not negligible in the lower half of the forest. Also in this region, canopy form drag destruction of $\overline{\langle w \rangle'^2}$ is negligible which differs from its significance in the budget of $\overline{\langle U \rangle'^2}$, $\overline{\langle V \rangle'^2}$, $\overline{\langle u \rangle'^2}$, and $\overline{\langle v \rangle'^2}$.

Half the pressure transport of $\overline{\langle w \rangle'^2}$ is the pressure transport of $\overline{\langle E \rangle}$ (the resolved-scale TKE) because its counterparts in the budgets of horizontal velocity variances are zero due to horizontal homogeneity. In contrast, turbulent transport is significant in the budgets of all velocity variances in the RSL above the forest and in the upper half of the forest. As a result, in this region, pressure transport is smaller than turbulent transport in the budget of $\overline{\langle E \rangle}$. However, the opposite is shown in the lower half of the forest. Our results on pressure transport are in agreement with earlier small-domain LESs of airflow in and above forest canopies (Dwyer et al. 1997) and direct numerical simulation (DNS) of an open-channel flow with sandgrain roughness (Yuan and Piomelli 2014). The opposite results have been previously reported based on wind-tunnel (Brunet et al. 1994) and flume experiment (Nepf and Vivoni 2000), in which the pressure transport was not directly measured and was set as the residual. Therefore, it is subject to errors in the estimates of the other terms in the TKE budget.

Finally, the pressure redistribution of normal stress is fairly constant with height in the lower half of the forest. Normalized values of R_{XX}, R_{YY}, R_{xx} and R_{yy} are all ~ 0.2 in the sparse ($VAI = 2$) model forest in LES Case 1, which indicates that pressure redistribution does not vary much with horizontal coordinate rotation. This follows earlier result in Sect. 3.2 that the values of $\overline{\langle U \rangle'^2}$, $\overline{\langle V \rangle'^2}$, $\overline{\langle u \rangle'^2}$ and $\overline{\langle v \rangle'^2}$ are very close to each other in the trunk space and do not vary much with height. Again, incompressibility ensures that the normalized value of R_{zz} is about -0.4. The above normalized values are reduced by approximately half in the dense ($VAI = 6.5$) model forest in LES Case 2 shown later in Fig. 8, as pressure transport of $\overline{\langle w \rangle'^2}$, the largest source in this region, is reduced by about half (Fig. 8c). The impact of LES domain and grid spacing on these values are discussed later in Sect. 3.7.

3.4 Budgets of Tangential Shear Stress

Following the similarities in the budgets of $\overline{\langle U\rangle'^2}$, $\overline{\langle V\rangle'^2}$ and $\overline{\langle u\rangle'^2}$, the budgets of $\overline{\langle U\rangle'\langle W\rangle'}$ (Fig. 6a), $\overline{\langle V\rangle'\langle W\rangle'}$ (Fig. 6b) and $\overline{\langle u\rangle'\langle w\rangle'}$ (Fig. 6c) are also similar, while terms in the budget of $\overline{\langle v\rangle'\langle w\rangle'}$ (Fig. 6d) are an order of magnitude smaller than their counterparts in the budget of $\overline{\langle u\rangle'\langle w\rangle'}$. Therefore, the discussion below is primarily on the budget of $\overline{\langle u\rangle'\langle w\rangle'}$.

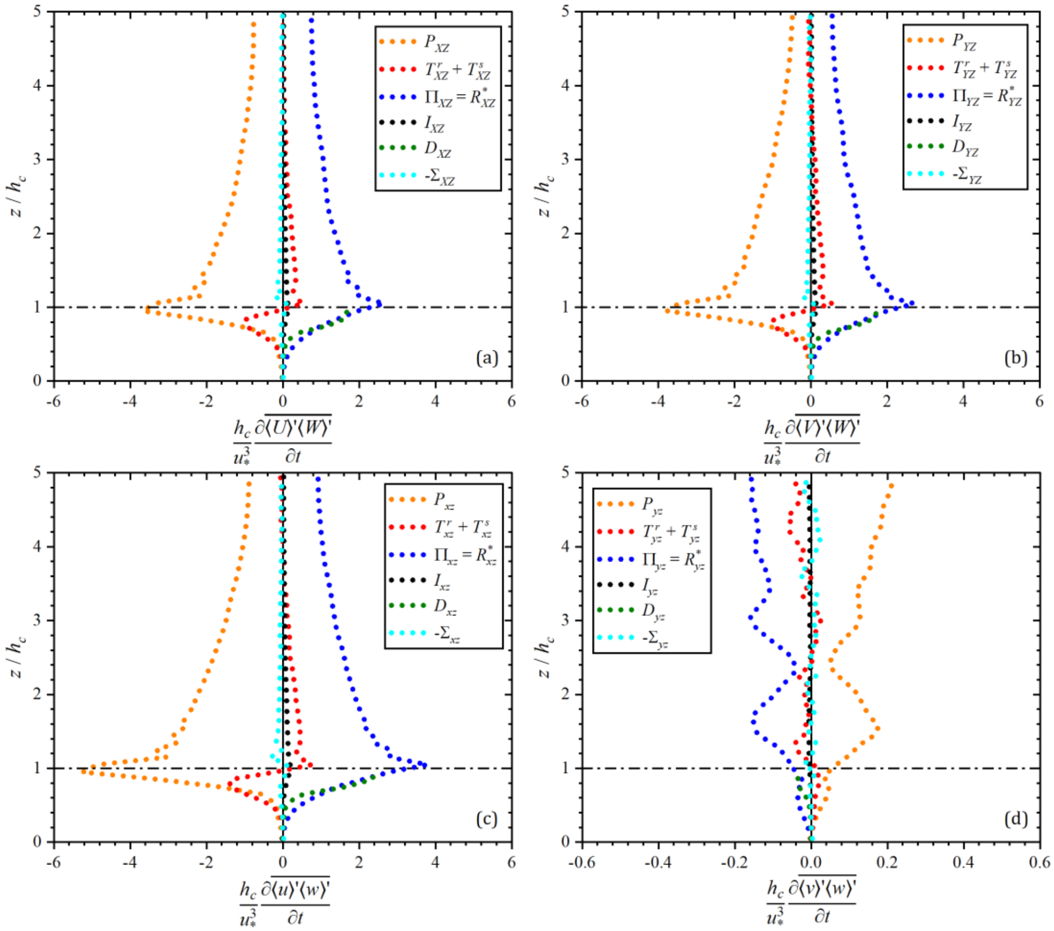

Fig. 6 A comparison of normalized budgets of the resolved-scale tangential shear stress between two horizontal coordinates (X, Y): (a) $\overline{\langle U\rangle'\langle W\rangle'}$; (b) $\overline{\langle V\rangle'\langle W\rangle'}$; and ($x$, y): (c) $\overline{\langle u\rangle'\langle w\rangle'}$; (d) $\overline{\langle v\rangle'\langle w\rangle'}$ for LES Case 1

Similar to the budgets of normal stress and TKE, turbulent transport ($T^r_{xz} + T^s_{xz}$) is a sink in the RSL above the forest with the maximum sink at the canopy top (Fig. 6c) and then generally decreases with increased altitude. It changed the $\pm$ sign at $z/h_c = 4$, above which is the ISL where the budget of $\overline{\langle u\rangle'\langle w\rangle'}$ is essentially a balance between shear production (P_{xz}) and pressure-gradient interaction ($\Pi_{xz} = R^*_{xz}$) as the only major sink. Inside the canopy, turbulent transport is also an important source in addition to shear production. The canopy form drag destruction (D_{xz}) is as an important sink as $\Pi_{xz} = R^*_{xz}$. Interscale transfer (I_{xz}) is negligible in the ISL and a much smaller sink than pressure-gradient interaction in the RSL. This is very different than its counterpart in the budgets of normal stresses.

Finally, despite the terms in the budget of $\overline{\langle v\rangle'\langle w\rangle'}$ are much smaller than their counterparts in the budget of $\overline{\langle u\rangle'\langle w\rangle'}$, the features concerning P_{yz}, $\Pi_{yz} = R^*_{yz}$, $T^r_{yz} + T^s_{yz}$, D_{yz}, and I_{yz} resemble those described above in the budgets of $\overline{\langle u\rangle'\langle w\rangle'}$. For example, shear production and pressure-gradient interaction are the largest source and sink, respectively. One difference is the opposite $\pm$ sign in corresponding terms as a result of $\overline{\langle v\rangle'\langle w\rangle'} > 0$ both in the RSL and in the ISL above (Fig. 3d).

3.5 Comparison between LESs and Field Observations

A brief comparison is presented here between the LESs of Su (1997) and Su et al. (1998a, 1998b, 2000) and the field observation in and above a deciduous forest at Camp Borden in 1986 that was used in Su et al. (1998a). Given the similarity in vegetation area density profiles between these two datasets (Fig. 1), LES Run D was chosen (Fig. 7) because it has the largest domain among the four earlier LES runs (Table 2). It should be noted that the LES budgets are for the resolved-scale turbulence only, whereas the field observations are based on time-averages of all observed eddy sizes down to the path-lengths among paired sonic transducers. Su et al. (2000) showed better agreement between the field observations and the LESs when the 10-Hz field data were filtered by a 3-s window (translating to a length scale close to the subfilter scale in the LESs using the mean wind speed at the treetops). The vertical spacings between adjacent measurement levels in the field are $0.26\ h_c$, $0.28\ h_c$, $0.13\ h_c$ inside the forest and $0.93\ h_c$ above the forest in the order from bottom up (Shaw et al. 1988). Only the results at $z/h_c = 0.94$ has a normalized vertical spacing close to the vertical grid spacing in LES Run D. Despite these differences, the overall agreements on normalized shear production, turbulent transport and destruction by canopy form drag are fairly good in the RSL. The largest relative differences appear to be at the lowest observation level $z/h_c = 0.47$. These results lend some credibility to the pressure-gradient interaction terms derived from the LESs that were not measured in the field. The experiment at Camp Borden only measured turbulent pressure perturbations at the ground surface (Shaw et al. 1990; Shaw and Zhang 1992), as was the case in a wheat field (Maitani and Seo 1985).

Despite LES Run D has the largest domain in both the vertical and horizontal directions among the four earlier small-domain LES runs (Table 2), the depth of the RSL are still smaller than that in the four large-domain LES cases (Table 1). For example, turbulent transport in the budget of $\overline{\langle E \rangle}$ changed the $\pm$ sign between $z/h_c = 2.65$ and 2.75 in LES Run D (Fig. 7d), whereas it is between $z/h_c = 3.75$ and 3.85 in LES Case 1 (Fig. 5f).

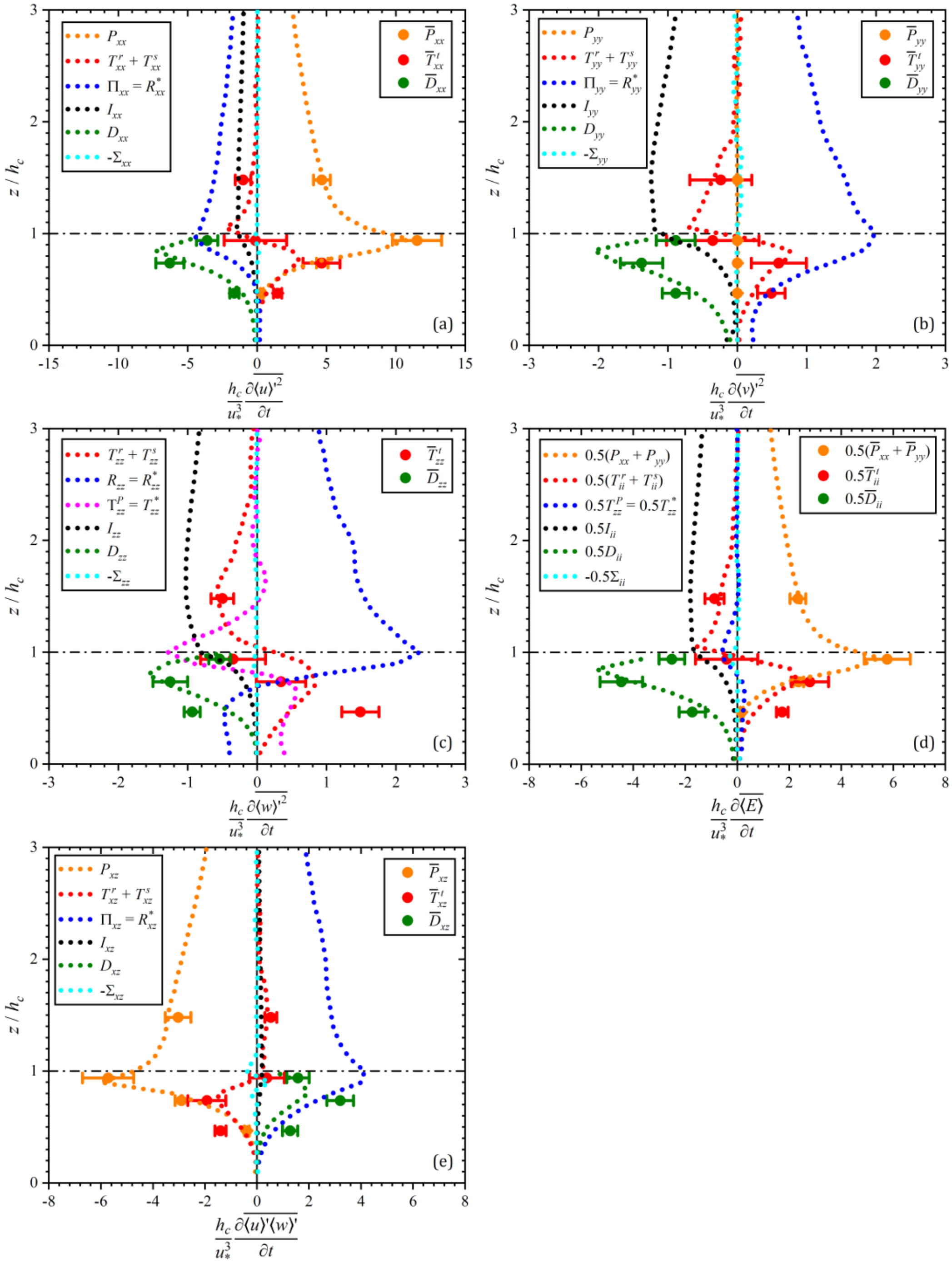

Fig. 7 Comparing normalized budgets of Reynolds stress and TKE between LES Run D (dotted lines) and field observation at Camp Borden in 1986 used in Su et al. (1998a) (filled circles with error bars): (a) $\overline{\langle u\rangle'^2}$; (b) $\overline{\langle v\rangle'^2}$; (c) $\overline{\langle w\rangle'^2}$; (d) $\overline{\langle E\rangle}$; (e) $\overline{\langle u\rangle'\langle w\rangle'}$. An overbar is added to the symbol for the same term to make the distinction that the field observations are based on time averages of observed turbulent scales, whereas the LES is for the resolved scales only, e.g., turbulent transport in the field observation is denoted by $\overline{T}_{ik}^{t}$

3.6 Effects of Vegetation Density and Geostrophic Wind Speed

Here we primarily use LES Case 1 ($VAI = 2$) and Case 2 ($VAI = 6.5$) to assess the effects of vegetation density on the resolved-scale Reynolds stress and TKE (Fig. 8). Although both LES Run D and LES Case 1 have an *LAI* or *VAI* of 2, they differ in leaf or vegetation area density in the upper portions of the forests (Fig. 1). Therefore, LES Run D may also be used. However, different domain sizes between LES Run D and LES Case 1 can also contribute to differences between them, which is discussed in the next section.

Increased vegetation density led to greater mean wind shear (Fig. 2d) and enhanced shear production (Fig. 8a, d, e) in the vicinity of the canopy top. This subsequently led to greater peak values of most budget terms in this region but in varying degrees. The largest enhancement is in normalized pressure transport such that both the peak sink above the canopy and the peak source inside the canopy are more than doubled (Fig. 8c, d). A smaller percentage but discernible enhancement in pressure transport of resolved-scale TKE due to increased leaf area density is also shown in the earlier small-domain LESs by Dwyer et al. (1997). Inside the canopy, peak values in both pressure transport and turbulent transport are located closer to the canopy top in the denser model forest (LES Case 2) by one vertical grid spacing. Above the canopy, the absolute differences in the same normalized budget term (shear production, interscale transfer, pressure redistribution or pressure-gradient interaction) between the two model forests decrease with increased height as the magnitudes of the budget terms decrease.

As expected, shear production, pressure redistribution or pressure-gradient interaction, canopy form drag destruction and interscale transfer attenuate more rapidly with increased depth into the canopy in the denser model forest. As a result, the same normalized budget term is greater in the top 20% of the denser forest, but is smaller below.

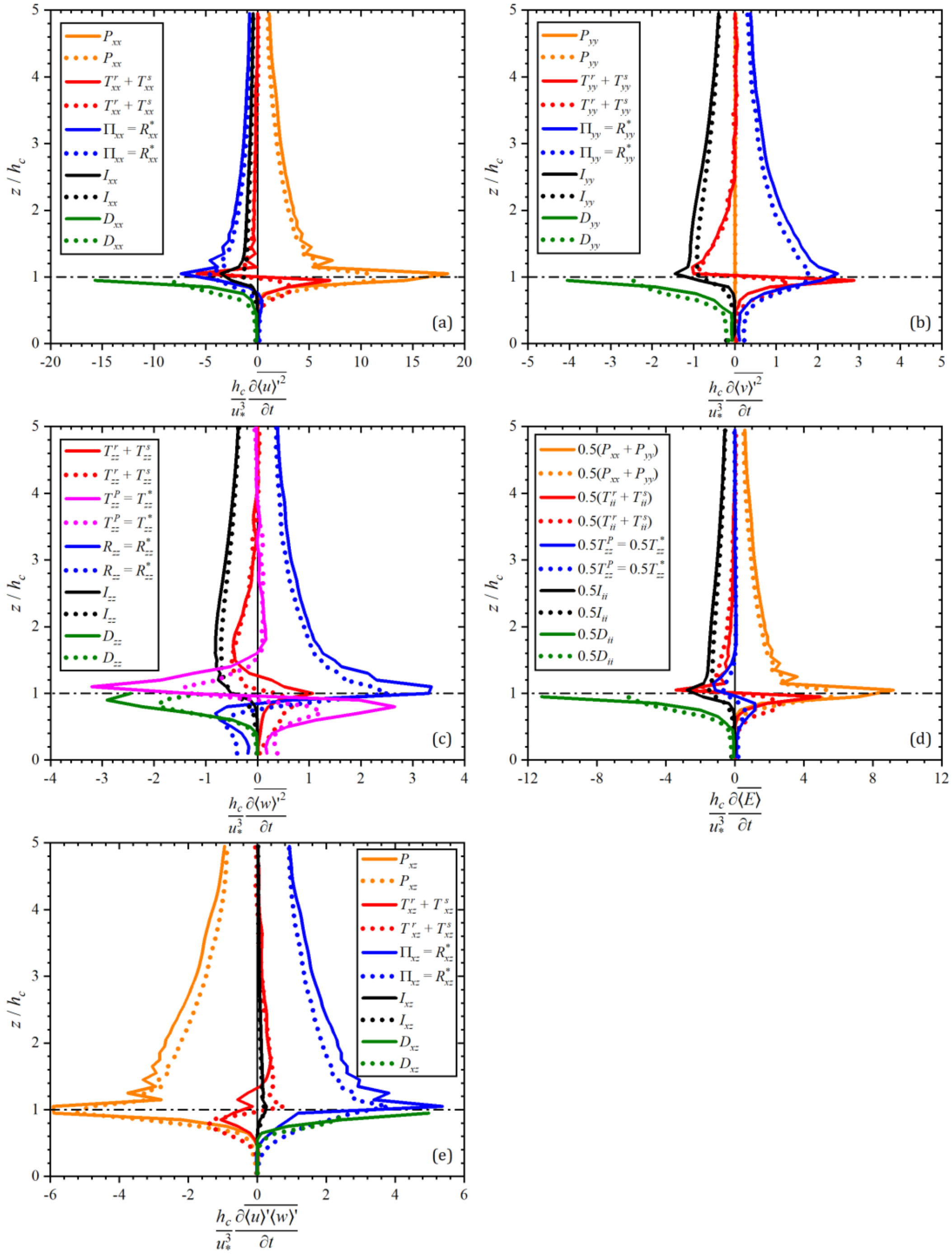

Fig. 8 Comparing normalized budgets of the resolved-scale Reynolds stress and TKE between LES Case 1 ($VAI = 2$, dotted lines) and LES Case 2 ($VAI = 6.5$, solid lines) in the (x, y, z) coordinate: (a) $\overline{\langle u \rangle'^2}$; (b) $\overline{\langle v \rangle'^2}$; (c) $\overline{\langle w \rangle'^2}$; (d) $\overline{\langle E \rangle}$; and (e) $\overline{\langle u \rangle' \langle w \rangle'}$

A less consistent picture is shown of turbulent transport, particularly in the budgets of $\overline{\langle w\rangle'^2}$ and $\overline{\langle u\rangle'\langle w\rangle'}$. Both $T^r_{zz} + T^s_{zz}$ and $T^r_{xz} + T^s_{xz}$ switched the $\pm$ sign at $z/h_c = 1.3$ over the dense forest but across the canopy top over the sparse forest (Fig. 8c, e). In contrast, both $T^r_{xx} + T^s_{xx}$, $T^r_{yy} + T^s_{yy}$ and $0.5(T^r_{ii} + T^s_{ii})$ changed the $\pm$ sign across the canopy top over both the dense and sparse model forests (Fig. 8a, b, d). This could also be due to inadequate vertical grid resolution discussed earlier in Sect. 3.2 on the kinks in Reynolds stress just above the dense model forest (LES Case 2) where the turbulent shear length scale is less than half of that over the sparse (LES Case 1) model forest (Table 1). Therefore, a greater burden is placed on the SFS parametrization which may be deficient for simulating very dense canopies with inadequate grid resolution.

Finally, the effects of geostrophic wind speed or external horizontal mean pressure-gradient force are much smaller than those of vegetation density, especially in the surface layer including both ISL and RSL. Normalized budgets terms are nearly indistinguishable between LES Case 1 and Case 3, or between LES Case 2 and Case 4 (Table 1). Therefore, they are not presented here.

3.7 Impacts of LES Domain Size and Grid Spacing

Here we primarily use LES Runs A, B, and D to evaluate the impact of domain size since they have the same grid spacing and leaf area density profile. We also include LES Case 1 for this discussion because it has the same grid spacing and *VAI* of 2 albeit a different vegetation area density profile (Fig. 1). The effect of grid spacing is assessed by comparing LES Runs A and C which have the same domain size and leaf area density profile. Following Su et al. (1998a), we focus on results in the RSL up to twice the canopy height, mainly due to the smallest vertical domain in LES Runs A and C.

Doubling the vertical domain in LES Run B in comparison to LES Run A reduced the magnitudes of non-transport budget terms above the canopy and in the top 20% of the forest. These include shear production P_{xx} (Fig. 9a) and P_{xz} (Fig. 9b), interscale transfer $0.5I_{ii}$ (Fig. 9c), pressure redistribution $\Pi_{xx} = R^*_{xx}$ (Fig. 10a), $\Pi_{yy} = R^*_{yy}$ (Fig. 10b) and $R_{zz} = R^*_{zz}$ (Fig. 10c), and pressure-gradient interaction $\Pi_{xz} = R^*_{xz}$ (Fig. 10d). The opposite is shown in canopy form drag destruction $0.5D_{ii}$ (Fig. 9d), in turbulent transport $0.5(T^r_{ii} +$

T_{ii}^{s}) both above and within the forest (Fig. 9e), and in pressure transport $T_{zz}^{p} = T_{zz}^{*}$ inside the forest (Fig. 9f). Note that the pressure redistribution, the pressure-gradient interaction and the pressure transport used here are defined in (8), (9), and (11).

The above impacts are further enhanced by doubling the horizontal domain in LES Run D in comparison to LES Run B, and in LES Case 1 which has the largest domain both in the horizontal and the vertical directions with a much greater ABL depth. However, the difference in vertical distribution of a_p between LES Case 1 and LES Run D (Fig. 1) also contributed to differences between the two, particularly in the upper portions of the canopy. The effect of a larger domain (LES Case 1) having led to greater depths of both the RSL and the ISL than LES Run D has been discussed earlier in Sect. 3.5. The depths of the RSL determined by turbulent transport are further suppressed by smaller horizontal domain in LES Run B and by smaller vertical domain in LES Runs A and C (Fig. 9e).

Reducing the grid spacing by half in LES Run C in comparison to LES Run A also enhanced shear production, interscale transfer, pressure redistribution and pressure-gradient interaction above the canopy and in the top 20% of the forest, particularly around the peaks near the canopy top. This is opposite to the impact of increased domain size. However, both a finer grid resolution and a larger domain enhanced canopy form drag destruction inside the canopy, as well as turbulent transport, including peak sink just above the canopy and peak source inside the canopy (Fig. 9e). In contrast, a finer grid resolution reduced pressure transport whereas a larger domain enhanced pressure transport in the lower 2/3 of the forest and above the canopy, except near the canopy top where a finer grid resolution yielded a greater sink in pressure transport.

In the lower half of the canopy, pressure redistribution of normal stress is enhanced with increased LES domain but reduced with decreased grid spacing (Fig. 10a, b, c). These are opposite to the impacts in the upper portions of the canopy and above the canopy. In addition, in the lower half of the forest, the impact of increased domain is greater than that of decreased grid spacing, whereas the two are comparable in the top 20% of the forest and above the canopy. In the lowest 1/3 of the sparse forest, among LES Runs A–D, only Run D yielded normalized values of R_{xx} and R_{yy} (~ 0.2) and of R_{zz} (about −0.4) that are close to those in LES Case 1 ($VAI = 2$) discussed earlier in Sect. 3.3 (Fig. 5).

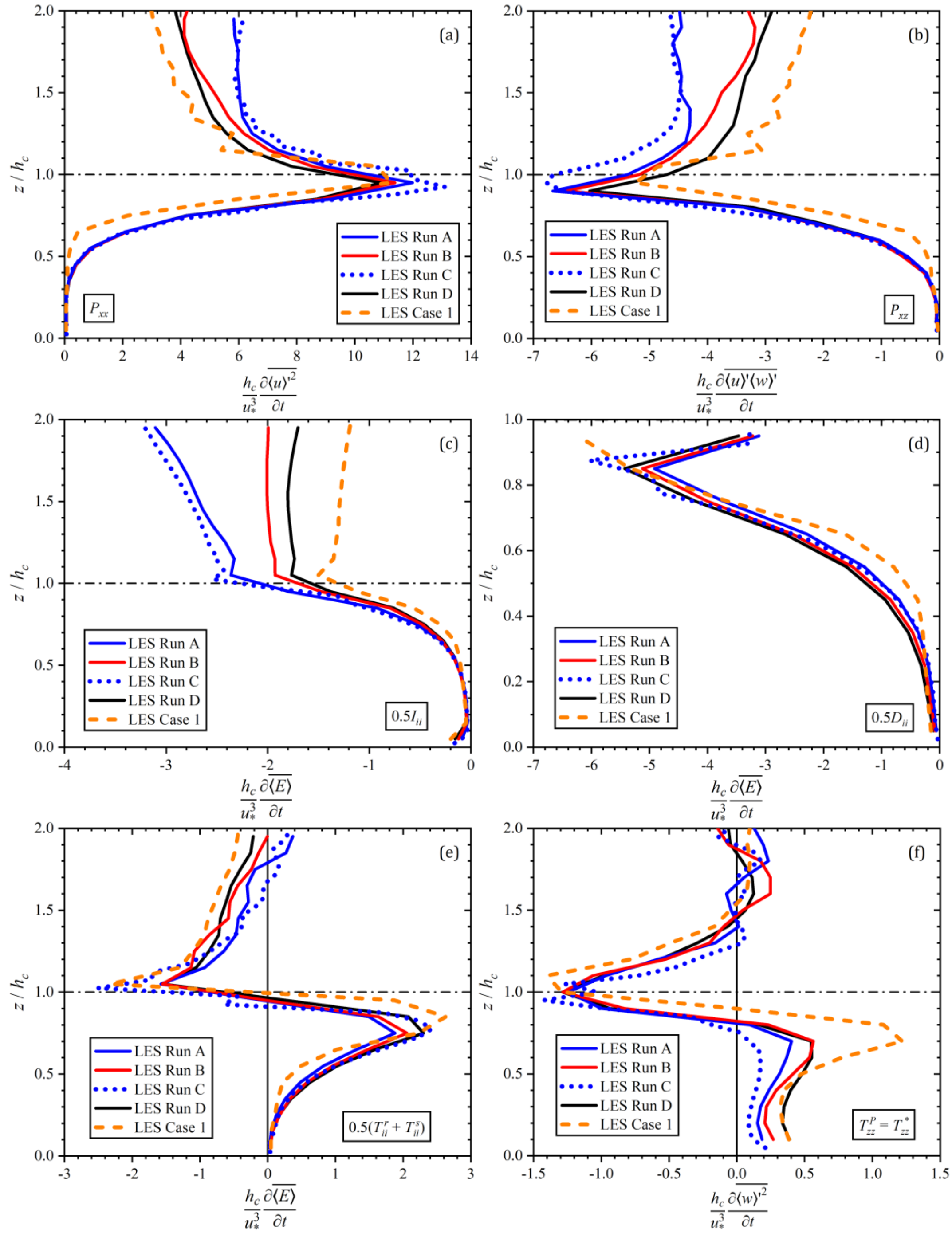

Fig. 9 Comparing LES Runs A–D and LES Case 1 to examine the effects of domain size, grid spacing, and vertical distribution of a_p on shear production (a) P_{xx} and (b) P_{xz}; interscale transfer (c) $0.5I_{ii}$; canopy form drag destruction (d) $0.5D_{ii}$; turbulent transport (e) $0.5(T_{ii}^r + T_{ii}^s)$; and pressure transport (f) $T_{zz}^p = T_{zz}^*$

Some of the artifacts due to the momentum source imposed in the top grids (Su et al. 1998a) shown in LES Runs A and C which have the smallest domain, are removed in LES Runs B and D up to at least twice the canopy height, and is not an issue in LES Case 1. These artifacts include that shear production (Fig. 9a, b) and pressure-redistribution (Fig. 10a, b, c) cease to decrease with increased height above $z/h_c = 1.5$, and that interscale transfer (Fig. 9c) and pressure-gradient interaction (Fig. 10d) increase with increased height above $z/h_c = 1.2$ and $z/h_c = 1.3$, respectively.

Finally, the depth of a layer in the RSL above the canopy in which pressure transport is a significant sink of $\overline{\langle w \rangle'^2}$ slightly increases with increased vertical domain and slightly decreases with reduced grid spacing (Fig. 9f).

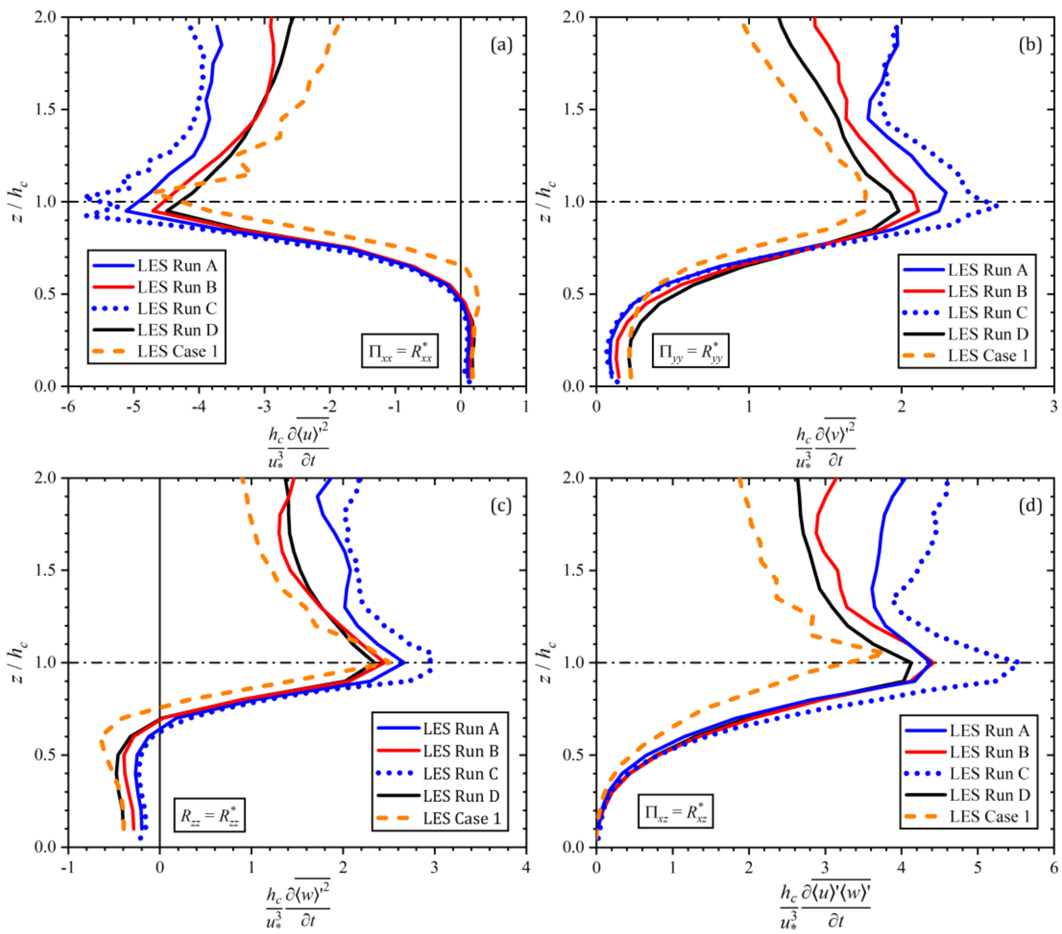

Fig. 10 Comparing LES Runs A–D and LES Case 1 to examine the effects of domain size, grid spacing, and vertical distribution of a_p on pressure redistribution (a) $\Pi_{xx} = R^*_{xx}$; (b) $\Pi_{yy} = R^*_{yy}$; (c) $R_{zz} = R^*_{zz}$; and pressure-gradient interaction (d) $\Pi_{xz} = R^*_{xz}$

4 Conclusions

The overarching goal of this paper is to expand our work on this subject first reported in a dissertation and a conference presentation based on a single LES Run A (Table 2) with the smallest LES domain over 20 years ago. The expanded work performed included analyses of three additional LES Runs B–D (Table 2) that have been previously used only to study two-point space-time correlations and coherent structures. Four LES cases of inversion-capped neutral ABLs with much larger domain and ABL depths similar to previous LESs of shear-driven ABLs while maintaining the same fine grid spacing are augmented to the analyses. These LES runs and cases allowed us to examine the effects of LES domain size and grid spacing. They also enabled us to study the effects of *VAI* or *LAI* and its vertical distribution, and of varying geostrophic wind speed. The evaluation of the budgets of all non-negligible Reynolds stress components together helped to fill a void in the literature on airflows in and above plant canopies in the atmospheric surface layer comprised of both the RSL and the ISL, although only in simple situations such as horizontally homogeneous forests over flat terrain.

One of the most important results is that in the upper portions of the canopy and above, pressure redistribution is a major sink of normal stress in horizontal direction with mean shear production as a major source, whereas in the horizontal direction that is absent of mean shear production and in the vertical direction, pressure redistribution is a major source of normal stress. However, in the lower half of the forests where both mean shear production and turbulent transport are diminished, pressure transport is the dominant source of vertical velocity variance and TKE, whereas pressure redistributions are major sources of horizontal velocity variances but a sink of vertical velocity variance. The fact that the results on pressure redistributions do not change with horizontal coordinate rotation supports earlier findings based on field observations (Shaw et al. 1990; Shaw and Zhang 1992) that horizontal velocity fluctuations in the trunk space are largely driven by pressure perturbations associated with coherent structures comprised of ejection and sweep. On the other hand, pressure transport is a major source of vertical velocity variance from the ground level to just under the treetops where it transitions to a major sink up to about 1.5 times canopy height, and is greater than turbulent transport in the same region. An interesting result in comparing the budgets of normal stress in the horizontal directions between the (X, Y, Z) and (x, y, z) coordinates is that in the surface layer above the forest, pressure redistribution is a bigger sink than interscale transfer in the budget of normal stress in the mean wind (x) direction, but the opposite is shown in the budgets of normal stresses in the east (X) and north (Y) directions. These results will be used in the evaluation of the parametrizations of pressure redistribution and pressure transport in a companion paper, in which different decompositions have been used, including (8)–(11) in this paper.

In this study, we used Reynolds stress budgets to discuss the depths of both the RSL (significance of turbulent transport and pressure transport) and the ISL (logarithmic layer and negligible transport). The depths of both the RSL and ISL are shown to increase with increased LES domain (Tables 1 and 2). For the same model forest (Table 2) and same LES grid spacing, increased LES domain in the vertical direction (LES Run B) and in the horizontal directions (LES Run D) led to increased turbulent shear length scales calculated at the canopy top. This is in agreement with the findings in Su et al. (2000) based on two-point space-time correlations and spatial integral turbulent length scales. In addition, the RSL is deeper and the turbulent shear length scale is greater (larger eddies) over the sparse (LES Case 1) forest than the dense (LES Case 2) forest (Table 1). A deficiency in our earlier LES Runs A and C is the enhanced shear production and interscale transfer that do not change with altitude between 1.5 to 2 times canopy height, which is an artifact due to the momentum source imposed in the top grids in the smallest vertical domain. This artifact is removed at least up to twice the canopy height with increased vertical domain in LES Runs B and D, and is not an issue at all in the 4 large-domain LES Cases 1–4.

Peak values of normalized major budget terms in the vicinity of the treetops increase with increased vegetation density, but change little with geostrophic wind speed for the same model forest. A stronger geostrophic wind speed leads to a deeper ABL but does not influence the normalized Reynolds stress budgets in the surface layer significantly, where the friction velocity and canopy height are used as characteristic velocity and length scales, respectively. The turbulent shear length scales are shown to decrease not only with increased *VAI* but also with increased a_p in the upper portions of the canopy for the same *LAI* or *VAI*, but change little with geostrophic wind speed for the same model forest. These results are in general agreement with previous studies (Raupach et al. 1996).

For the same sparse model forest (LES Runs A–D), increased domain size and reduced grid spacing generally enhance normalized budget terms near the treetops and above. The differences are comparable with variability in field observations which may be for different reasons such as varying ABL depths and mesoscale influences that are absent in the LESs.

We propose a new decomposition for the pressure-gradient interaction term that is consistent with the classic decomposition for the normal stress but is consistent with Lumley's decomposition for the tangential shear stress. The results reported here on the pressure-gradient interaction term will be further discussed in the evaluation of their parametrizations in existing higher-order closure models in a companion paper. These include not only discussions on the various decompositions of the pressure-gradient interaction term, but also seeking new parametrization schemes since there is no a priori mathematical reason to require the pressure-gradient velocity interaction to resemble a Cauchy type stress tensor amenable to deviatoric and transport parts. The value of this work lies in the significance of pressure redistribution in the budget of the normal stress (Fig. 5c, d, e) and of pressure-gradient interaction in the budget of tangential shear stress (Fig. 6) in both the RSL and the ISL.

Obviously, our simulations are not able to produce the very long (commonly exceeding 20 times boundary-layer depth) meandering "superstructures" in the logarithmic region (Hutchins and Marusic 2007). Efforts in applying LES to simulate these very-large-scale motions in neutrally stratified ABLs used a horizontal domain in the streamwise direction 8π times (Jacob and Anderson 2017) to 32π times (Fang and Port´e-Agel 2015) of the vertical domain. However, the finest grids (49.1, 49.1, 7.8) m in both studies have a very large aspect ratio of 2π:1, and could suffer the inherent problem of inadequately resolving the surface layer that includes the logarithmic region (Brasseur and Wei 2010; Ercolani et al. 2017). The effects of these very large superstructures on the results presented here remain to be studied when computational resources become available to us, along with thermal stability and a wider range of canopy morphology and vegetation density. Increased available computation resources would also allow us to further investigate airflow in the RSL in and above very dense forests where finer grid resolutions are needed to adequately resolve eddies near the canopy top with much reduced turbulent shear length scales.

Acknowledgements The first author would like to acknowledge and thank the US National Science Foundation (NSF), Division of Atmospheric and Geospace Sciences (AGS), Physical and Dynamic Meteorology Program, for their funding support through project AGS-0840191, as well as high-performance computing support from Yellowstone (ark:/85065/d7wd3xhc) provided by the Computational and Information Systems Laboratory (CISL) of the National Centre of Atmospheric Research (NCAR), which is sponsored by NSF. A mixed MPI-OpenMP LES code is provided by Dr. Edward Patton and Dr. Peter Sullivan at NCAR. The first author would also like to thank Siddhartha Ghosh of CISL for his technical support during the revisions of the LES code for running on Yellowstone. We thank the anonymous reviewers for their critical comments that helped to improve the quality of this paper. The authors declare that we have no conflict of interest to disclose.

Data availability Statement The datasets generated during and/or analysed during the current study are available from the corresponding author on reasonable request.

Appendix 1:

Selected full boundary-layer profiles of second-order statistics (Fig. 11d, e, f) are provided here to demonstrate fully developed turbulent inversion-capped (Fig. 11a, b) neutral ABLs. Figure 11 also helps to illustrate the large differences in the ABL height z_i determined by maximum $\partial\overline{\langle\theta\rangle}/\partial z$ (Fig. 11b) and by the minimum (peak negative) heat fluxes (Fig. 11e).

We may use the difference between the two estimates of z_i (minimum heat flux and maximum $\partial\overline{\langle\theta\rangle}/\partial z$) as an approximate measure of the depth of the capping inversion or interfacial layer between the well-mixed layer below and the stable free atmosphere above. Our LES results indicate that a stronger geostrophic wind or external horizontal pressure-gradient force led to an increased depth of this capping inversion layer (Fig. 11a, b, e). This increase is primarily due to the increase in the altitude of maximum $\partial\overline{\langle\theta\rangle}/\partial z$ (Fig. 11b), which represents the entrainment interface between the ABL and the free atmosphere above (Sullivan et al. 1998). The depth of this capping inversion layer is much smaller in Berg et al. (2020), which could be due to a number of factors: (1) a much lower geostrophic wind (5 m s^{-1}); (2) half the inversion strength (3 K km^{-1}) in the free atmosphere above the ABL; and (3) over a much smoother surface (z_0 = 0.05 m). The maximum $\partial\overline{\langle\theta\rangle}/\partial z$ (~ 30 K km^{-1}) in our study (Fig. 11b) is twice that (~ 15 K km^{-1}) in simulation D in Berg et al. (2020).

A well-mixed layer can be seen above the surface layer and below the altitude of minimum heat flux. It is characterized by near-uniform $\overline{\langle\theta\rangle}$ (Fig. 11a), quasi-linear increase in the magnitude of negative heat flux with increased altitude (Fig. 11e), and horizontal wind direction angle decreases with increased altitude at nearly a constant rate that is smaller than those both inside the canopy (Fig. 2e) and in the capping inversion layer (Fig. 11c). Similar features are shown in Fig. 11 and Fig. 10 in Berg et al. (2020).

Snapshots in an X-z plane of turbulent velocities and momentum and heat fluxes (Fig. 12) also help to illustrate a fully developed turbulent ABL. While the most significant local heat fluxes (Fig. 12d) are found in the capping inversion layer (Fig. 11b), the largest local momentum fluxes (Fig. 12c) are shown in the ABL below. The horizontal scales of fluctuating turbulent velocities are larger in the interior of the ABL and decreased towards both the forest and the ABL top (Fig. 12a, b; Fig. 13a–e; and Fig. 14a–e), especially the horizontal velocities.

The two-dimensional spectra (Fig. 13f and Fig. 14f) are averaged (Sullivan and Patton 2011; Patton et al. 2016; Berg et al. 2020) but more precisely integrated at constant horizontal wavenumber $\kappa_h = \left(\kappa_X^2 + \kappa_Y^2\right)^{1/2}$ along a circular ring over respective two-dimensional power spectra that are functions of wavenumbers $\left(\kappa_X, \kappa_Y\right)$ in the X- and Y-directions. These spectra are more representative of the spatial eddy scales than their one-dimensional counterparts which are contaminated by aliasing from average (again, more precisely integration over κ_X or κ_Y) in either the X- or Y-directions (Wyngaard 2010).

We present the spectra at the same five normalized height (z/h_c = 0.5, 1, 2, 6, 10) as in Patton et al. (2016) for comparison with their near-neutral (NN) case. The difference in magnitudes of the normalized spectra between the present study (Fig. 13f and Fig. 14f) and their counter parts (Fig. 8) in Patton et al. (2016) are due to differences in both the velocity scale (u_*^2 in this study but $w_m^2 = 5.358\, u_*^2$ in Patton et al. 2016) and in the length scale L_x, which in this study is 1/5 of that in Patton et al. (2016). The limit of smaller horizontal domain in the present study is manifested by the spectral peak being located at the lowest wavenumber for the streamwise velocity (Fig. 13f) at $z/h_c = 10$, which is well above the RSL. At this altitude ($z/z_i = 0.20$), similar to Patton et al. (2016), both the streamwise (Fig. 13f) and the vertical (Fig. 14f) velocity spectra generally show the −5/3 slope. At $z/h_c = 6$ ($z/z_i = 0.12$), the streamwise velocity spectra peaked at a lower wavenumber than the vertical velocity spectra. This is also the case at $z/h_c = 0.5$, 1, 2 in the RSL in and above the forest. Other features similar to Patton et al. (2016) include: (1) energy at low wavenumbers diminishes as the canopy top is approached from $z/h_c = 2$ to $z/h_c = 1$; (2) spectra at mid-canopy ($z/h_c = 0.5$) maintain a similar shape to those at the canopy top but diminished in magnitude by a factor of 5 to 10; and (3) the peak in vertical velocity spectra in the RSL ($z/h_c = 0.5$, 1, 2) is between $\kappa_h h_c = 1$ and $\kappa_h h_c = 2$. The horizontal scales and magnitudes of the normalized spectra are also manifested in the horizontal snapshots of the streamwise (Fig. 13a−e) and vertical (Fig. 14a−e) velocities at the same altitude.

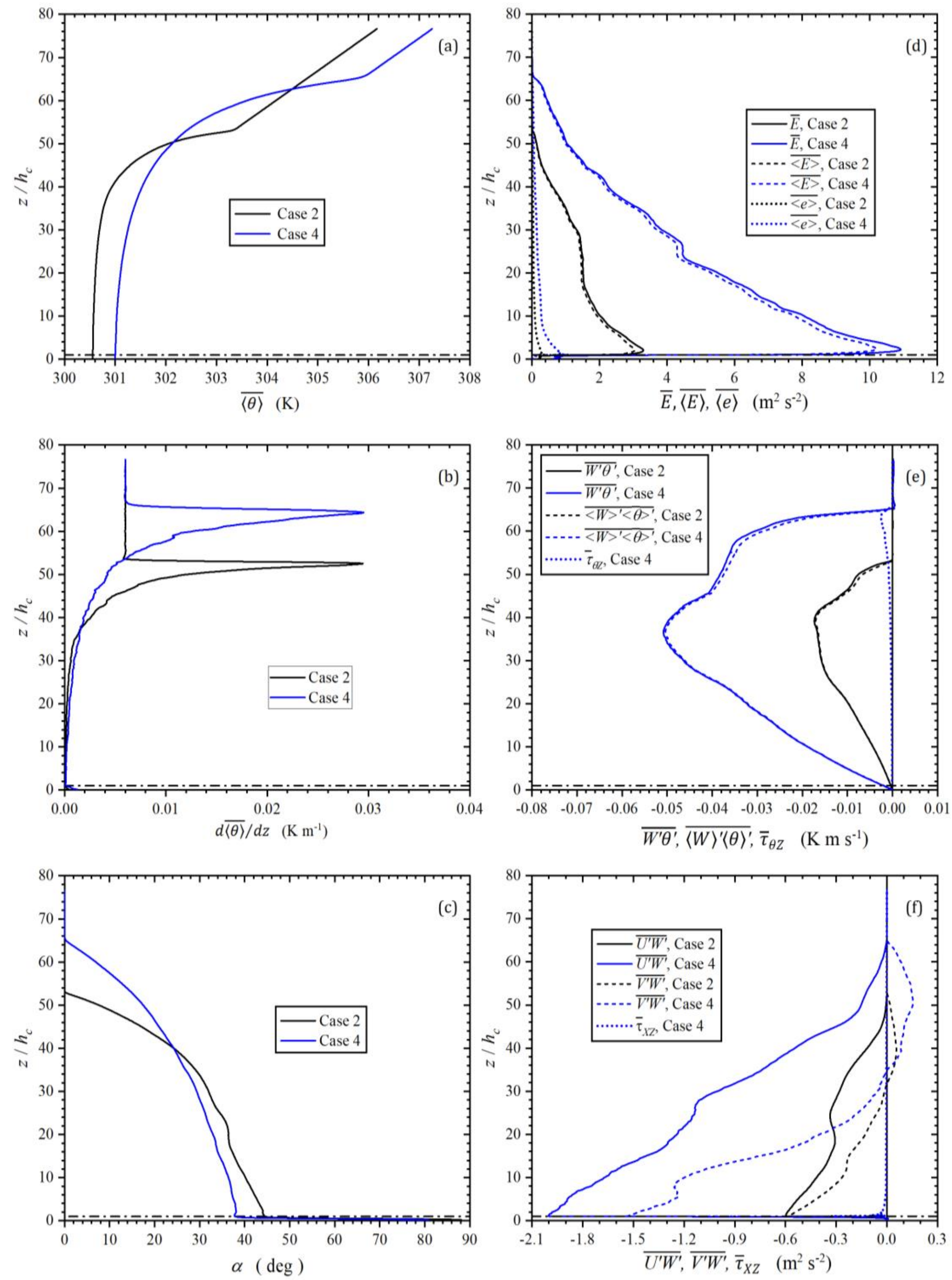

Fig. 11 Full ABL Profiles of: (a) $\overline{\langle\theta\rangle}$; (b) $\partial\overline{\langle\theta\rangle}/\partial z$; (c) horizontal mean wind directional angle α counter-clockwise from the east; (d) resolved-scale TKE $\overline{\langle E\rangle}$, SFS TKE $\overline{\langle e\rangle}$, $\overline{E} = \overline{\langle E\rangle} + \overline{\langle e\rangle}$; (e) resolved-scale heat flux $\overline{\langle w\rangle'\langle\theta\rangle'}$, SFS heat flux $\overline{\tau}_{\theta z}$, $\overline{w'\theta'} = \overline{\langle w\rangle'\langle\theta\rangle'} + \overline{\tau}_{\theta z}$; (f) $\overline{U'W'} = \overline{\langle U\rangle'\langle W\rangle'} + \overline{\tau}_{XZ}$ and $\overline{V'W'} = \overline{\langle V\rangle'\langle W\rangle'} + \overline{\tau}_{YZ}$, in which $\overline{\langle U\rangle'\langle W\rangle'}$ and $\overline{\langle V\rangle'\langle W\rangle'}$ are the resolved-scale shear stresses, only SFS shear stress $\overline{\tau}_{XZ}$ for LES Case 4 is shown for the sake of clarity

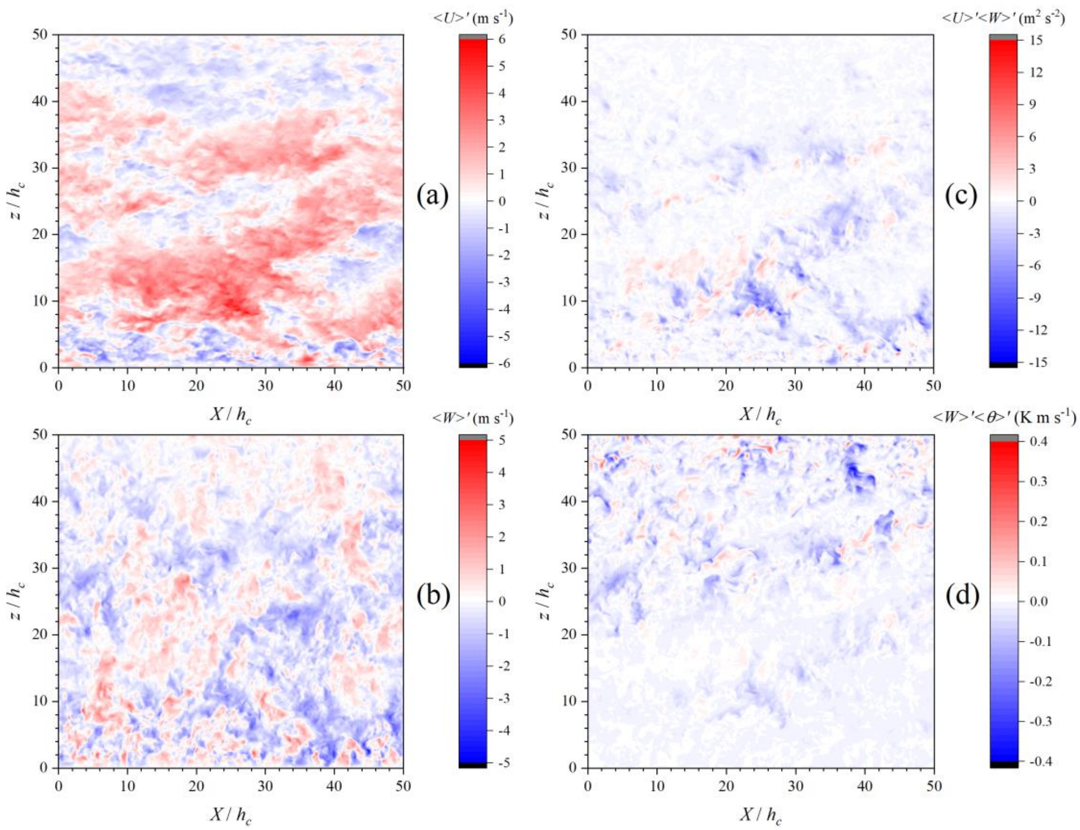

Fig. 12 Snapshots in an *X*-*z* plane in the middle of the *Y*-domain of turbulent velocities (from horizontal mean) and local shear stress and heat flux: (a) $\langle U\rangle'$, (b) $\langle W\rangle'$, (c) $\langle U\rangle'\langle W\rangle'$, (d) $\langle W\rangle'\langle\theta\rangle'$, for LES Case 1

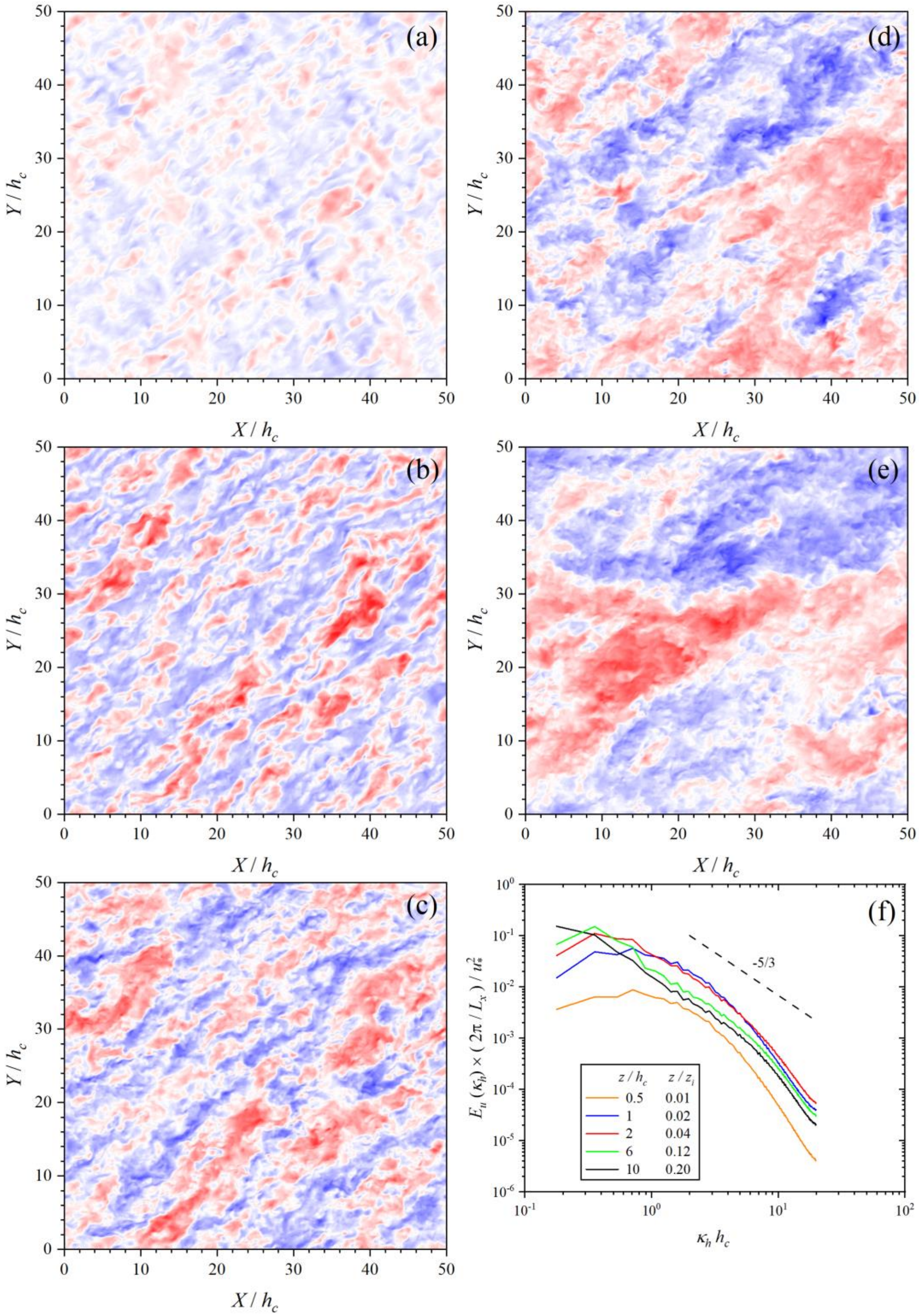

Fig. 13 Snapshots in the *X*-*Y* plane of turbulent fluctuations (from horizontal mean) of $\langle U\rangle'$ at: (a) $z/h_c = 0.5$, (b) $z/h_c = 1$, (c) $z/h_c = 2$, (d) $z/h_c = 6$ and (e) $z/h_c = 10$; (f) two-dimensional normalized energy spectra of streamwise velocity as a function of horizontal wavenumber κ_h, for LES Case 1. The same contour level in Fig. 12a is applied in panels (a)–(e)

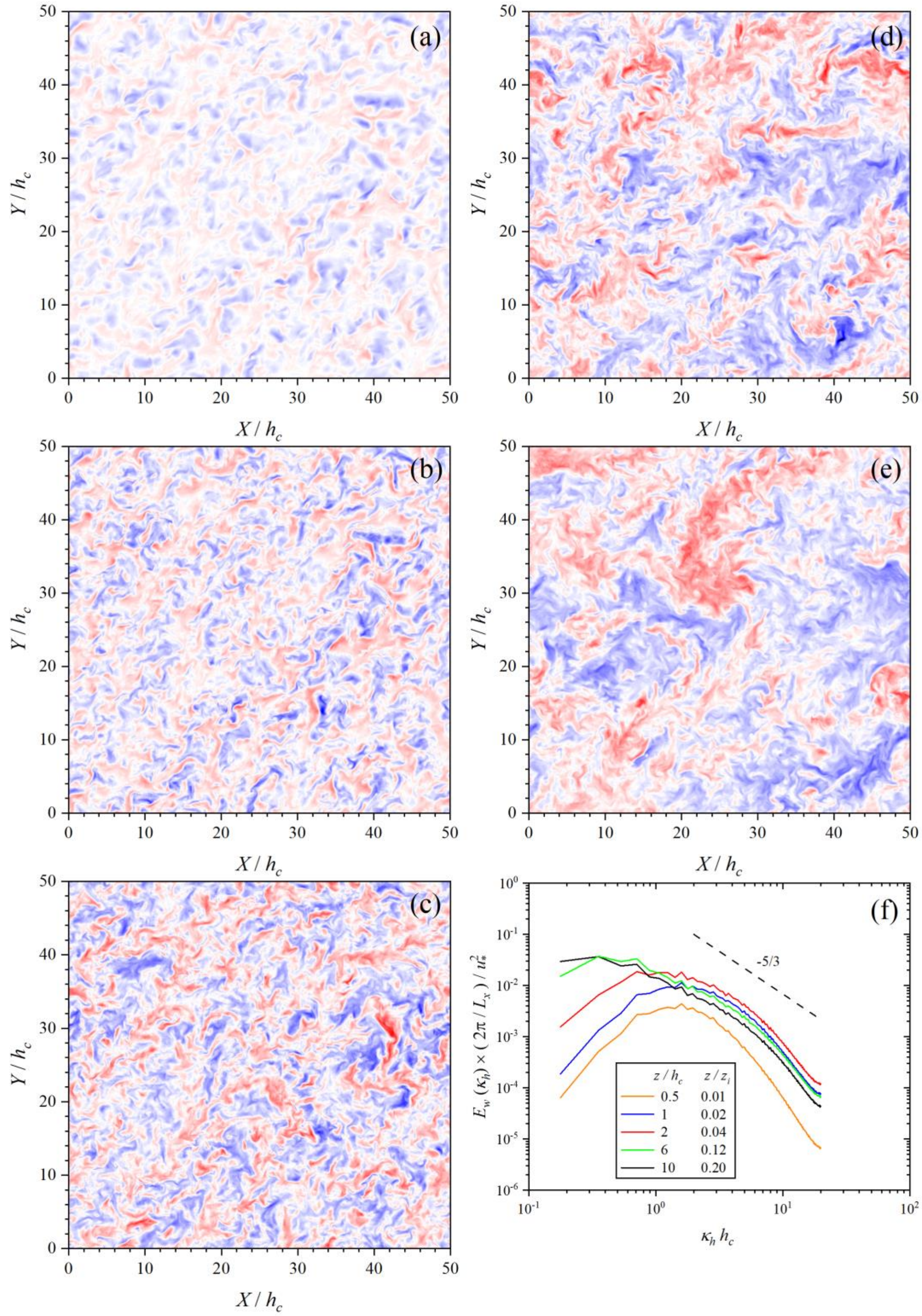

Fig. 14 Snapshots in the *X*-*Y* plane of turbulent vertical velocity ⟨*W*⟩' at: (a) $z/h_c = 0.5$, (b) $z/h_c = 1$, (c) $z/h_c = 2$, (d) $z/h_c = 6$ and (e) $z/h_c = 10$; (f) two-dimensional normalized energy spectra of vertical velocity as a function of horizontal wavenumber κ_h, for LES Case 1. The same contour level in Fig. 12b is applied in panels (a)–(e)

References

Albertson JD, Katul GG, Wiberg P (2001) Relative importance of local and regional controls on coupled water, carbon and energy fluxes. Adv. Water Resourc 24: 1103–1118

Andrén A, Moeng C-H (1993) Single-point closures in a neutrally stratified boundary layer. J Atmos Sci 50:3366–3379

Ayotte KW, Finnigan JJ, Raupach MR (1999) A second-order closure for neutrally stratified vegetative canopy flows. Boundary-Layer Meteorol 90:189–216

Bailey BN, Stoll R (2013) Turbulence in sparse, organized vegetative canopies: a large-eddy simulation study. Boundary-Layer Meteorol 147:369–400

Bailey BN, Stoll R (2016) The creation and evolution of coherent structures in plant canopy flows and their role in turbulent transport. J Fluid Mech 789:425–460

Baldocchi DD, Hutchison BA (1987) Turbulence in an almond orchard. Boundary-Layer Meteorol 40:127–146

Baldocchi DD, Meyers TP (1988) Turbulence structure in a deciduous forest. Boundary-Layer Meteorol 43:345–364

Banerjee T, De Roo F, Mauder M (2017) Connecting the failure of K theory inside and above vegetation canopies and ejection–sweep cycles by a large-eddy simulation. J Appl Meteorol Clim 56: 3119–3131, doi:10.1175/JAMC-D-16-0363.1.

Berg J, Patton EG, Sullivan PP (2020) Large-eddy simulation of conditionally neutral boundary layers: a mesh resolution sensitivity study. J Atmos Sci 77:1969-1991

Blunn LP, Coceal O, Nazarian N, Barlow JF, Plant RS, Bohnenstengel SI, Lean HW (2022) Turbulence characteristics across a range of idealized urban canopy geometries. Boundary-Layer Meteorol 182: 275–307

Bohrer G, Katul GG, Walko RL, Avissar R (2009) Exploring the effects of microscale structural heterogeneity of forest canopies using large-eddy simulation. Boundary-Layer Meteorol 132:351-382

Boudreault LÉ, Dupont S, Bechmann A, Dellwik E (2017) How forest inhomogeneities affect the edge flow. Boundary-Layer Meteorol 162:375–400

Brasseur JG, Wei T (2010) Designing large-eddy simulation of the turbulent boundary layer to capture law-of-the-wall scaling. Phys Fluids 22: 021303

Brunet Y, Raupach MR, Finnigan JJ (1994) A wind tunnel study of air flow in waving wheat: Single-point velocity statistics. Boundary-Layer Meteorol 70:95-132

Cassiani M, Katul GG, Albertson JD (2008) The effects of canopy leaf area index on airflow across forest edges: large-eddy simulation and analytical results. Boundary-Layer Meteorol 126:433–460

Chahine A, Dupont S, Sinfort C, Brunet Y (2014) Wind-flow dynamics over a vineyard. Boundary-Layer Meteorol 151:557–577

Chatziefstratiou EK, Velissariou V, Bohrer G (2014) Resolving the effects of aperture and volume restriction of the flow by semi-porous barriers using large-eddy simulations. Boundary-Layer Meteorol 152:329–348

Deardorff JW (1972) Numerical investigation of neutral and unstable planetary boundary layers. J Atmos Sci 29:91-115

Deardorff JW (1973a) Three-dimensional numerical modeling of the planetary boundary layer. In: Haugen DA (ed) Workshop on micrometeorology. American Meteorological Society, pp 271–311

Deardorff JW (1973b) The use of subgrid transport equations in a three-dimensional model of atmospheric turbulence. J Fluids Eng Trans ASME 429-438

Donaldson C duP (1973) Construction of a dynamic model of the production of atmospheric turbulence and the dispersal of atmospheric pollutants. In: Haugen DA (ed) Workshop on micrometeorology. American Meteorological Society, pp 313–392

Dupont S, Brunet Y (2008a) Edge flow and canopy structure: a large-eddy simulation study. Boundary-Layer Meteorol 126:51-71

Dupont S, Brunet Y (2008b) Influence of foliage density profile on canopy flow: A large-eddy simulation study. Agric For Meteorol 148:976-990

Dupont S, Brunet Y, Finnigan JJ (2008) Large-eddy simulation of turbulent flow over a forested hill: validation and coherent structure identification. Q J R Meteorol Soc 134:1911-1929

Dupont S, Brunet Y (2009) Coherent structures in canopy edge flow: a large-eddy simulation study. J Fluid Mech 630:93–128

Dupont S, Gosselin F, Py C, de Langre E, Hemon P, Brunet Y (2010) Modeling waving crops using large-eddy simulation: comparison with experiments and a linear stability analysis. J Fluid Mech 652: 5-44

Dupont S, Bonnefond JM, Irvine MR, Lamaud E, Brunet Y (2011) Long-distance edge effects in a pine forest with a deep and sparse trunk space: in situ and numerical experiments. Agric For Meteorol 151:328–344

Dupont S, Irvine MR, Bonnefond JM, Lamaud E, Brunet Y (2012) Turbulent structures in a pine forest with a deep and sparse trunk space: stand and edge regions. Boundary-Layer Meteorol 143:309–336

Dupont S, Patton EG (2012) Influence of stability and seasonal canopy changes on micrometeorology within and above an orchard canopy: The CAHTS experiment. Agric For Meteorol 157:11–29

Dwyer MJ, Patton EG, Shaw RH (1997) Turbulent kinetic energy budgets from a large-eddy simulation of airflow above and within a forest canopy. Boundary-Layer Meteorol 84:23-43

Ercolani G, Gorlé C, Corbari C, Mancini M (2017) RAMS sensitivity to grid spacing and grid aspect ratio in large-eddy simulations of the dry neutral atmospheric boundary layer. Comput Fluids 146: 59–73

Fang J, Port´e-Agel F (2015) Large-eddy simulation of very-large-scale motions in the neutrally stratified atmospheric boundary layer. Boundary-Layer Meteorol 155: 397–416

Finnigan JJ (2000) Turbulence in plant canopies. Annu Rev Fluid Mech 32:519-571

Finnigan JJ, Shaw RH, Patton EG (2009) Turbulence structure above a vegetation canopy. J Fluid Mech 637:387-424

Fitzmaurice L, Shaw RH, Paw U KT, Patton EG (2004) Three-dimensional scalar microfornt system in a large-eddy simulation of vegetation canopy flow. Boundary-Layer Meteorol 112:107-127

Gardiner BA (1994) Wind and wind forces in a plantation spruce forest. Boundary-Layer Meteorol 67:161-186

Garratt JR (1992) The atmospheric boundary layer. Cambridge University Press, Cambridge, 316 pp

Gavrilov K, Morvan D, Accary G, Lyubimov D, Meradji S (2013) Numerical simulation of coherent turbulent structures and of passive scalar dispersion in a canopy sub-layer. Computers Fluids 78:54-62

Giometto MG, Christen A, Meneveau C, Fang J, Krafczyk M, Parlange MB (2016) Spatial characteristics of roughness sublayer mean flow and turbulence over a realistic urban surface. Boundary-Layer Meteorol 160: 425–452

Graham J, Meneveau C (2012) Modelling turbulent flow over fractal trees using renormalized numerical simulation: Alternate formulations and numerical experiments. Phys Fluids 24:125105

Groth J (1991) Description of the pressure effects in the Reynolds stress transport equations. Phys Fluids A3(9):2276-2277

Hanjalić K, Launder BE (1972) Fully developed asymmetric flow in a plane channel. J Fluid Mech 51:301-335

Hanjalić K, Launder B (2011) Modelling turbulence in engineering and the environment, second-moment routes to closure. Cambridge University Press, Cambridge, 379 pp

Heinze R, Mironov D, Raasch S (2015) Second-moment budgets in cloud-topped boundary layers: A large-eddy simulation study. J Adv Model Earth Syst 7:510–536, doi:10.1002/2014MS000376

Heinze R, Mironov D, Raasch S (2016) Analysis of pressure-strain and pressure gradient-scalar covariances in cloud-topped boundary layers: A large-eddy simulation study. J Adv Model Earth Syst 8:3–30, doi:10.1002/2015MS0000508

Holton JR, Hakim GJ (2012) An introduction to dynamic meteorology. 5th Ed. Academic Press, 532 pp

Huang J, Cassiani M, Albertson JD (2009) The effects of vegetation density on coherent turbulent structures within the canopy sublayer: a large-eddy simulation study. Boundary-Layer Meteorol 133:253–275

Huang J, Cassiani M, Albertson JD (2011) Coherent turbulent structures across a vegetation discontinuity. Boundary-Layer Meteorol 140:1–22

Hutchins N, Marusic I (2007) Evidence of very long meandering features in the logarithmic region of turbulent boundary layers. J Fluid Mech 579: 1-28

Jackson PS (1981) On the displacement height in the logarithmic velocity profile. J Fluid Mech 111:15-25

Jacob C, Anderson W (2017) Conditionally averaged large-scale motions in the neutral atmospheric boundary layer: insights for aeolian processes. Boundary-Layer Meteorol 162: 21–41

Jiménez J (2004) Turbulent flows over rough walls. Annu Rev Fluid Mech 36:173-196

Kaimal JC, Finnigan JJ (1994) Atmospheric boundary layer, their structure and measurement. Oxford University Press, Cambridge, 289 pp

Kanda M, Hino M (1994) Organized structures in developing turbulent flow within and above a plant canopy, using a large-eddy simulation. Boundary-Layer Meteorol 68:237–257

Katul GG, Albertson JD (1998) An investigation of higher-order closure models for a forested canopy. Boundary-Layer Meteorol 89:47-74

Launder BE, Reece GJ, Rodi W (1975) Progress in the development of a Reynolds-stress turbulence closure. J Fluid Mech 68: 537-566

Leclerc MY, Beissner KC, Shaw RH, den Hartog G, Neumann HH (1990) The influence of atmospheric stability on the budgets of the Reynolds stress and turbulent kinetic energy within and above a deciduous forest. J Appl Meteorol 29:916–933

Lin C-L, Moeng C-H, Sullivan PP, McWilliams JC (1997) The effect of surface roughness on flow structures in a neutrally stratified planetary boundary layer flow. Phys Fluids 9(11):3235-3249

Liu Z, Hu Y, Fan Y, Wang W, Zhou Q (2019) Turbulent flow fields over a 3D hill covered by vegetation canopy through large eddy simulations. Energies 12(19):3624

Lopes AS, Palma JML, Piomelli U (2015) On the determination of effective aerodynamic roughness of structures with vegetation patches. Boundary-Layer Meteorol 156:113–130

Lumley JL (1975) Pressure-strain correlation. Phys Fluids 18:750

Lumley JL, Khajeh-Nouri B (1975) Computational modeling of turbulent transport. Adv Geophys 18(A):169-192

Lumley JL (1979) Computational modelling of turbulent flows. Adv Applied Mech 18: 123-176

Ma Y, Liu H, Liu Z, Yi C, Lamb B (2020) Influence of forest-edge flows on scalar transport with different vertical distributions of foliage and scalar sources. Boundary-Layer Meteorol 174:99-117

Maitani T, Seo T (1985) Estimates of velocity-pressure and velocity-pressure gradient interactions in the surface layer over plant canopies. Boundary-Layer Meteorol 33:51-60

Mansour NN, Kim J, Moin P (1988) Reynolds-stress and dissipation-rate budgets in a turbulent channel flow. J Fluid Mech 194:15-44

Mellor GL (1973) Analytic prediction of the properties of stratified planetary surface layers. J Atmos Sci 30:1061–1069

Mellor GL, Yamada T (1974) A hierarchy of turbulence closure models for planetary boundary layers. J Atmos Sci 31:1791–1806

Mellor GL, Yamada T (1982) Development of a turbulence closure model for geophysical fluid problems. Rev Geophys Space Phys 20:851–875

Moeng C-H (1984) A large-eddy-simulation model for the study of planetary boundary-layer turbulence. J Atmos Sci 41:2052–2062

Moeng C-H, Wyngaard JC (1988) Spectral analysis of large-eddy simulations of the convective boundary layer. J Atmos Sci 45:3573–3587

Moeng C-H, Sullivan PP (1994) A comparison of shear- and buoyancy-driven planetary boundary layer flows. J Atmos Sci 51:999–1022

Meyers T, Paw U KT (1986) Testing of a higher-order closure model for modeling airflow within and above plant canopies. Boundary-Layer Meteorol 37:297-311

Meyers T, Baldocchi DD (1991) The budgets of turbulent kinetic energy and Reynolds stress within and above a deciduous forest. Agric For Meteorol 53:207-222

Nakao K, Hattori Y (2019) Effect of the granularity of heterogeneous forest cover on the drag coefficient. Boundary-Layer Meteorol 170:235–255

Nazarian N, Krayenhoff ES, Martilli A (2020) A one-dimensional model of turbulent flow through "urban" canopies (MLUCM v2.0): updates based on large-eddy simulation. Geosci Model Dev 13: 937–953

Nebenführ B, Davidson L (2015) Large-eddy simulation study of thermally stratified canopy. Boundary-Layer Meteorol 156:253–276

Nepf HM, Vivoni ER (2000) Flow structure in depth-limited, vegetated flow. J Geophys Res 105(C12):28,547-28,557

Neumann HH, Den Hartog G, Shaw RH (1989) Leaf area measurements based on hemispheric photographs and leaf-litter collection in a deciduous forest during autumn leaf-fall. Agric For Meteorol 45:325-345

Ouwersloot HG, Moene AFM, Attema JJ, de Arellano JVG (2017) Large-eddy simulation comparison of neutral flow over a canopy: sensitivities to physical and numerical conditions, and similarity to other representations. Boundary-Layer Meteorol 162:71–89

Pan Y, Chamecki M, Isard SA (2014a) Large-eddy simulation of turbulence and particle dispersion inside the canopy roughness sublayer. J Fluid Mech 753: 499–534

Pan Y, Follett E, Chamecki M, Nepf H (2014b) Strong and weak, unsteady reconfiguration and its impact on turbulence structure within plant canopies. Phys. Fluids 26 (10): 105102, doi:10.1063/1.4898395

Panofsky HA (1973) Tower micrometeorology. In: Haugen DA (ed) Workshop on micrometeorology. American Meteorological Society, pp 151–176

Patton EG, Shaw RH, Judd MJ, Raupach MR (1998) Large-eddy simulation of windbreak flow. Boundary-Layer Meteorol 87:275-306

Patton EG, Sullivan PP, Davis KJ (2003) The influence of a forest canopy on top-down and bottom-up diffusion in the planetary boundary layer. Q J R Meteorol Soc 129:1415-1434

Patton EG, Katul GG (2009) Turbulent pressure and velocity perturbations induced by gentle hills covered with sparse and dense canopies. Boundary-Layer Meteorol 133:189-217

Patton EG, Coauthors (2011) The canopy horizontal array turbulence study. Bull Amer Meteorol Soc 92: 593–611

Patton EG, Sullivan PP, Shaw RH, Finnigan JJ, Weil JC (2016) Atmospheric stability influences on coupled boundary layer and canopy turbulence. J Atmos Sci 73:1621-1647

Pedersen JG, Gryning SE, HG, Kelly M (2014) On the structure and adjustment of inversion-capped neutral atmospheric boundary-layer flows: large-eddy simulation study. Boundary-Layer Meteorol 153:43–62

Poggi D, Katul GG, Albertson JD (2004) Momentum transfer and turbulent kinetic energy budgets within a dense model canopy. Boundary-Layer Meteorol 111:589–614

Pope SB (2000) Turbulent flows. Cambridge University Press, Cambridge, 771 pp

Pyles DR, Paw U KT, Falk M (2004) Directional wind shear in an old-growth temperate forest: observations and model results. Agric For Meteorol 125:19-31

Raupach MR, Coppin PA, Legg BJ (1986) Experiments on scalar dispersion within a model plant canopy. Part I: The turbulence structure. Boundary-Layer Meteorol 35:21-52

Raupach MR, Finnigan JJ, Brunet Y (1996) Coherent eddies and turbulence in vegetation canopies: The mixing-layer analogy. Boundary-Layer Meteorol 78:351-382

Ross AN (2011) Scalar transport over forested hills. Boundary-Layer Meteorol 141:179-199

Rotta, JC (1951) Statistische theorie nichthomogener turbulenz. Z Phys 129: 547-572

Rudnicki M, Mitchell SJ, Novak MD (2004) Wind tunnel measurements of crown streamlining and drag relationships for three conifer species. Can J For Res 34: 666-676

Salesky ST, Chamecki M, Bou-Zeid E (2017) On the nature of the transition between roll and cellular organization in the convective boundary layer. Boundary-Layer Meteorol 163:41–68

Schmid HP, Su H-B, Vogel CS, Curtis PS (2003) Ecosystem-atmosphere exchange of carbon dioxide over a mixed hardwood forest in northern lower Michigan. J Geophys Res 108(D14): 4417 doi:10.1029/2002JD003011

Schlegel F, Stiller J, Bienert A, Maas H-G, Queck R, Bernhofer C (2012) Large-eddy simulation of inhomogeneous canopy flows using high resolution terrestrial laser scanning data. Boundary-Layer Meteorol 142:223–243

Schlegel F, Stiller J, Bienert A, Maas H-G, Queck R, Bernhofer C (2015) Large-eddy simulation study of the effects of a heterogeneous forest at sub-tree resolution. Boundary-Layer Meteorol 154:27–56

Schröttle J, Dörnbrack A (2013) Turbulence structure in a diabatically heated forest canopy composed of fractal Pythagoras trees. Theor Comput Fluid Dyn 27:337–359

Shaw RH, Seginer I (1985) The dissipation of turbulence in plant canopies. Preprint, American Meteorological Society’s 7th Symposium on Turbulence and Diffusion, 200-203, Boulder, CO.

Shaw RH, den Hartog G, Newmann HH (1988) Influence of foliar density and thermal stability on profiles of Reynolds stress and turbulence intensity in a deciduous forest. Boundary-Layer Meteorol 45:391-409

Shaw RH, Patton EG (2003) Canopy element influences on resolved- and subgrid-scale energy within a large-eddy simulation. Agric For Meteorol 115:5-17

Shaw RH, Paw U KT, Zhang XJ, Gao W, den Hartog G, Newmann HH (1990) Retrieval of turbulent pressure fluctuations at the ground surface beneath a forest. Boundary-Layer Meteorol 50:319-338

Shaw RH, Schumann U (1992) Large-eddy simulation of turbulent flow above and within a forest. Boundary-Layer Meteorol 61:47-64

Shaw RH, Zhang XJ (1992) Evidence of pressure-forced turbulent flow in a forest. Boundary-Layer Meteorol 58:273-288

Shaw RH, Brunet Y, Finnigan JJ, Raupach MR (1995) A wind tunnel study of air flow in waving wheat: Two-point velocity statistics. Boundary-Layer Meteorol 76:349-376

Shen S, Leclerc MY (1997) Modelling the turbulence structure in the canopy layer. Agric For Meteorol 87:3-25
Stull RB (1988) An introduction to boundary layer meteorology. Kluwer Academic Publishers, the Netherlands, 666 pp
Su H-B (1997) Numerical simulation of plant-atmosphere interactions using large-eddy simulation and coupled leaf and canopy models. Ph.D. dissertation, University of California, Davis, California, USA
Su H-B, Leclerc MY (1998) Large-eddy simulation of tracer footprints from infinite crosswind line sources inside a forest. Preprint, American Meteorological Society 23rd Conference on Agricultural and Forest, 388-391, Albuquerque, NM
Su H-B, Shaw RH, Paw U KT, Moeng C-H, Sullivan PP (1998a) Turbulent statistics of neutrally stratified flow within and above a sparse forest from large-eddy simulation and field observations. Boundary-Layer Meteorol 88:363-397
Su H-B, Shaw RH, Paw U KT, Moeng C-H (1998b) Large-eddy simulation of pressure-gradient-velocity covariance and its parameterization within and above a forest. Preprint, American Meteorological Society 23rd Conference on Agricultural and Forest, 229-232, Albuquerque, NM
Su H-B, Shaw RH, Paw U KT (2000) Two-point correlation analysis of neutrally stratified flow within and above a forest from large-eddy simulation. Boundary-Layer Meteorol 94:423-460
Su H-B, Schmid HP, Vogel CS, Curtis PS (2008) Effects of canopy morphology and thermal stability on mean flow and turbulent statistics observed inside a mixed hardwood forest. Agric For Meteorol 148:862-882
Sullivan PP, McWilliams JC, Moeng C-H (1994) A subgrid-scale model for large-eddy simulation of planetary boundary-layer flows. Boundary-Layer Meteorol 71:247-276
Sullivan PP, McWilliams JC, Moeng C-H (1996) A grid nesting method for large-eddy simulation of planetary boundary layer flows. Boundary-Layer Meteorol 80:167-202
Sullivan PP, Moeng C-H, Stevens B, Lenschow DH, Mayor SD (1998) Structure of the entrainment zone capping the convective atmospheric boundary layer. J Atmos Sci 55:3042–3064
Sullivan PP, Patton EG (2011) The effect of mesh resolution on convective boundary layer statistics and structures generated by large-eddy simulation. J Atmos Sci 68:2395-2415
Sun W-Y, Ogura Y (1980) Modeling the evolution of the convective planetary boundary layer. J Atmos Sci 37:1558–1572
Thom AS (1971) Momentum absorption by vegetation. Quart J Roy Meteorol Soc 97:414-428
van Hout R, Zhu W-H, Luznik L, Katz J, Kleissl J, Parlange MB (2007) PIV measurements in the atmospheric boundary layer within and above a mature corn canopy. Part I: Statistics and energy flux. J Atmos Sci 55:3042–3064
Vollsinger S, Mitchell SJ, Byrne KE, Novak MD, Rudnicki M (2005) Wind tunnel measurements of crown streamlining and drag relationships for several hardwood species. Can J For Res 35: 1238-1249

Watanabe T (2004) Large-eddy simulation of coherent turbulence structures associated with scalar ramps over plant canopies. Boundary-Layer Meteorol 112:307–341

Watanabe T (2009) LES study on the structure of coherent eddies inducing predominant perturbations in velocities in the roughness sublayer over plant canopies. J Meteorol Soc Japan 87:39–56

Watanabe T, Shimoyama K, Kawashima M, Mizoguchi Y, Inagaki A (2020) Large-eddy simulation of neutrally-stratified turbulent flow within and above plant canopy using the central-moments-based lattice Boltzmann method. Boundary-Layer Meteorol 176:35–60

Weligepolage K, Gieske ASM, van der Tol C, Timmermans J, Su Z (2012) Effect of sub-layer corrections on the roughness parameterization of a Douglas fir forest. Agric For Meteorol 162-163:115–126

Wilson JD (1988) A second-order closure model for flow through vegetation. Boundary-Layer Meteorol 42:371-392

Wilson NR, Shaw RH (1977) A higher order closure model for canopy flow. J Applied Meteorol 16:1197–1205

Wyngaard JC (2010) Turbulence in the atmosphere. Cambridge University Press, Cambridge, 393 pp

Yamada T (1982) A numerical model study of turbulent airflow in and above a forest canopy. J Meteorol Soc Jpn 60(1):439–454

Yang B, Raupach MR, Shaw RH, Paw U KT, Morse AP (2006a) Large-eddy simulation of turbulent flow across a forest edge. Part I: flow statistics. Boundary-Layer Meteorol 120:377–412

Yang B, Morse AP, Shaw RH, Paw U KT, (2006b) Large-eddy simulation of turbulent flow across a forest edge. Part II: momentum and turbulent kinetic energy budgets. Boundary-Layer Meteorol 121:433–457

Yang B, Shaw RH, Paw UKT (2006c) Wind loading on trees across a forest edge: a large eddy simulation. Agric For Meteorol 141(2):133–146

Yue W, Parlange MB, Meneveau C, Zhu W-H, van Hout R, Katz J (2007) Large-eddy simulation of plant canopy flows using plant-scale representation. Boundary-Layer Meteorol 124:183–203

Yuan J., Piomelli U (2014) Roughness effects on the Reynolds stress budgets in near-wall turbulence. J Fluid Mech 760: R1, doi:10.1017/jfm.2014.608.

Yue W, Meneveau C, Parlange MB, Zhu W-H, Kang HS, Katz J (2008) Turbulent kinetic energy budgets in a model canopy: comparisons between LES and wind-tunnel experiments. Environ Fluid Mech 8:73–95

Zeman O, Lumley JL (1976) Modeling buoyancy driven mixed layers. J Atmos Sci 33:1974–1988